



# Assessment of vegetation water dynamics by comparing microwave remote sensing signals from satellites and field-based GNSS reflectometry

Andrew F. Feldman<sup>1,2</sup>, William K. Smith<sup>3</sup>, Alexandra G. Konings<sup>4</sup>, Martin J. Baur<sup>5</sup>, Marvin Browne<sup>4</sup>,  
5 David Chaparro<sup>6</sup>, Charles Devine<sup>3</sup>, Jennifer L. Diehl<sup>1,2</sup>, Arthur Endsley<sup>7</sup>, Thomas Jagdhuber<sup>8,9</sup>, Kristine  
M. Larson<sup>10</sup>, Coral del Mar Valle-Rodriguez<sup>11</sup>, Konstantin Schellenberg<sup>12,13</sup>, Ruxandra-Maria Zotta<sup>14</sup>,  
Shawn P. Serbin<sup>1</sup>

<sup>1</sup>Biospheric Sciences Laboratory, NASA Goddard Space Flight Center, Greenbelt, MD, USA

10 <sup>2</sup>Earth System Science Interdisciplinary Center, University of Maryland, College Park, MD, USA

<sup>3</sup>School of Natural Resources and the Environment, University of Arizona, Tucson, Arizona, USA

<sup>4</sup>Department of Earth System Science, Stanford University, Stanford, California, USA

<sup>5</sup>Department of Environmental Systems Science, ETH Zurich, Zurich, Switzerland

<sup>6</sup>CREAF, Cerdanyola del Valles, 08193 Barcelona, Spain

15 <sup>7</sup>Numerical Terradynamic Simulation Group, University of Montana, Missoula, MT, USA

<sup>8</sup>Microwaves and Radar Institute, German Aerospace Center (DLR), Oberpfaffenhofen, Germany

<sup>9</sup>Institute of Geography, University of Augsburg, Augsburg, Germany

<sup>10</sup>Department of Aerospace Engineering Sciences, University of Colorado, Boulder, CO, USA

<sup>11</sup>Department of Ecology and Evolutionary Biology, Cornell University, Ithaca NY, USA

20 <sup>12</sup>Department Biogeochemical Processes, Max Planck Institute for Biogeochemistry, Jena, Germany

<sup>13</sup>Department of Earth Observation, Friedrich Schiller University Jena, Jena, Germany

<sup>14</sup>Department for Geodesy and Geoinformation, TU Wien, Vienna, Austria

*Correspondence to:* Andrew F. Feldman (afeld24@umd.edu)

**Abstract.** Monitoring plant water stress and biomass is limited by labor intensive measurements techniques. Observing plant  
25 water conditions more broadly is now enabled by microwave remote sensing. Specifically, satellite-based vegetation optical  
depth (VOD) provides daily observations of vegetation water volume at tens of kilometers. While satellite VOD has been used  
for many applications, VOD validations have rarely been carried out. A new method has enabled direct measurements of in-  
situ VOD, from Global Navigation Satellite Systems (GNSS). However, GNSS measurements have yet to be applied to more  
globally dominant grasslands and shrublands. Here, we explore how satellite-based VOD from SMAP and AMSR-2 compares  
30 with field-based microwave observations from 272 GNSS-based interferometric reflectometry (GNSS-IR) sites across the  
Western U.S as a part of the Plate Boundary Observatory (PBO) H2O network. These sensors measure a proxy for VOD at a  
scale of tens of meters, the normalized microwave reflectance index (NMRI). We find that satellite VOD generally positively  
correlates with GNSS NMRI with correlations between 0.2 to 0.6 across sites. These correlations increase to 0.3 to 0.7 when  
evaluating sites in regions with low spatial vegetation type heterogeneity, low tree cover, and large seasonal vegetation  
35 dynamics. The correlations are higher for X-band VOD, likely related to our finding that both X-band VOD and NMRI are  
both more sensitive to seasonal vegetation variations than C-band and L-band VOD products. These findings suggest that



satellite VOD is capturing field-based GNSS signals in dryland ecosystems, and therefore that these sensors are a critical resource for validating satellite VOD at scale.

## 40 **1. Introduction**

Vegetation regulates the water, carbon, and energy cycles at the land surface, and thus is integral to the Earth system (Gentine et al., 2019). For example, transpiration accounts for most of land water flux to the atmosphere and vegetation also alters the surface radiative balance and lower-atmosphere aerodynamics (Good et al., 2015; Wang et al., 2014). Therefore, vegetation structure and function influences lower atmospheric processes and rainfall events through land-atmosphere interactions (Green et al., 2017; Taylor et al., 2012). Natural and cultivated plants also have societal importance in supporting food security by yielding crops and forage, as well as supporting recreation (Briske et al., 2023). If vegetation dries sufficiently, it also becomes fuel for wildfire, especially in drier locations like the Western U.S. (Orland et al., 2025). It is therefore critical to widely monitor vegetation water stress and seasonal vegetation biomass changes.

50 Many satellite-based optical vegetation indices have been used to evaluate upper canopy biomass, phenology, and ecosystem productivity (Smith et al., 2019; Tucker, 1979). For example, a primary variable for fire risk assessment, the live fuel moisture content, is commonly derived from satellite optical measurements (Yebra et al., 2013). However, these indices are largely limited by cloud cover and are sensitive only to the top-of-canopy leaves (Zeng et al., 2022). This prevents their applicability for evaluating plant hydraulics, water stress, and full canopy biomass, which requires sensitivity to water content of the full canopy and more rapid temporal sampling (otherwise reduced by cloud cover).

A more recent advance has been the use of passive microwave retrievals of vegetation water content, via an index called vegetation optical depth (VOD) (Konings et al., 2019). VOD represents the overall attenuation of the surface microwave emissions due to the vegetation canopy. VOD has the advantage of being unaffected by clouds and of being sensitive to different canopy layers, with the sensing depth increasing from mainly leaves at high frequencies (X-band; ~10 GHz) to additionally the branches and trunks across the entire canopy depth at low frequencies (L-band; 1.4 GHz). The microwave vegetation signal (via VOD) was initially considered a noise source as a part of retrievals of satellite soil moisture. However, with its value in providing internal vegetation water information, VOD is now more commonly retrieved along with soil moisture across NASA's Soil Moisture Active Passive (SMAP) mission, JAXA's Advanced Microwave Scanning Radiometer (AMSR) missions, and the European Space Agency's Soil Moisture and Ocean Salinity (SMOS) mission (Konings et al., 2017; Wigneron et al., 2017; Zotta et al., 2024). As a result, the ecosystem sciences community has rapidly embraced the use of VOD over the last decade across applications, including (but not limited to) wildfire fuel load, crop yield estimation, tree mortality, aboveground biomass and carbon storage, plant water stress, and plant hydraulic traits (Anderegg et al., 2020; Brandt et al., 2018; Chaparro et al., 2018; Feldman et al., 2021c; Felton et al., 2024; Konings and Gentine, 2017; Liu et al., 2021; Tian



70 et al., 2018). Since passive microwave retrievals have a coarse spatial resolution (~30 km), such applications are implemented at regional to global scales.

However, satellite-based VOD datasets, and the related vegetation water content variable, have not been widely validated. This stands in contrast to satellite-based soil moisture for which public agencies implemented soil moisture core calibration and validation sites and field campaigns (for example, the SMAP mission and its SMAPVEX campaigns) (Chan et al., 2016; 75 Colliander et al., 2017). In part, these field-based validation efforts were explicitly built into the mission requirements to achieve required levels of performance of soil moisture. VOD is largely not considered a part of these mission level requirements. Moreover, VOD faces substantial validation challenges compared to most other variables. First, VOD is a microwave metric that depends on both dry biomass and relative water content (Momen et al., 2017), and thus presents a challenge for measuring both of these properties in-situ requiring labor intensive and/or expensive techniques (Feldman, 2024). 80 Additionally, passive microwave radiometers' low measurement resolution (30km) presents the need to represent heterogeneity at the pixel scale. Therefore, a sufficient in-situ VOD validation configuration would require a substantial investment in widespread water potential measurements and dry biomass measurements across a 30 km scale, many of which may need to be measured manually and/or at a large cost.

85 Despite these limitations, some site-level validation efforts have been carried out to link in-situ measured VOD with canopy properties, especially using tower-mounted radiometers (Holtzman et al., 2021; Jackson and Schmugge, 1991). In these cases, tower-based radiometers are often mounted in a downward-looking configuration, with a caveat that they require partitioning of soil moisture and VOD similarly to the satellite scale. In some cases, the soil signal can be removed by covering the soil with a perfect reflector or isolating it within the VOD retrieval by directly measuring soil moisture in-situ (Meyer et al., 2018). 90 Nevertheless, both wheat field and forested sites show promise that radiometer VOD is detecting both leaf water potential dynamics and seasonal scale changes in biomass (Holtzman et al., 2021; Meyer et al., 2018). Additionally, observing system simulation experiments (OSSEs) have been conducted to evaluate algorithmic noise sources in VOD, at least pinpointing that newer VOD retrieval algorithms, especially those that regularize VOD, are reducing VOD error variance (Crow and Feldman, 2025; Dong et al., 2018; Feldman et al., 2021). Co-use of plant hydraulic models with VOD has also been used as a feasible 95 method to interpret the satellite VOD signal, especially the influence of dew on VOD (Feldman et al., 2021c; Xu et al., 2021; Yao et al., 2024). Nevertheless, these validation efforts remain limited and have not kept pace with the ecosystem science community's use of VOD. Ultimately, these field experiments need to evolve to a point at which VOD retrieval algorithms can be calibrated. Specifically, validation information is necessary to inform how to reduce VOD errors in joint retrievals with soil moisture as well as understand the influences of the mean and time dynamics of scattering albedo, first order scattering, 100 and surface roughness effects (Baur et al., 2019, 2021; Kurum et al., 2011).

An emerging, lower cost, and less labor-intensive technique that is increasingly being implemented at the field scale relies on global navigation satellite system (GNSS) sensors. An increasingly popular configuration for VOD validation is GNSS-



transmissometry (GNSS-T) approach, which positions a GNSS receiver above and below the canopy and estimates VOD as  
105 the signal difference (Humphrey and Frankenberg, 2023; Kesselring et al., 2025; Kurum et al., 2022). These configurations  
are typically deployed in forests with the below canopy GNSS receiver positioned above the ground to partially avoid  
interference from microwave soil reflectance, thus requiring the observed vegetation to be taller in stature. These sensors have  
been used in a dry forest in southern California (Humphrey and Frankenberg, 2023), temperate forest in Missouri, USA (Yao  
et al., 2024), high elevation cold forest in Colorado, USA (Burns et al., 2025), among other ongoing installations. These sites  
110 have continued to establish the relationship of VOD with relative water content, leaf water potential, transpiration, and biomass.  
A similar GNSS-T configuration has included mobile vehicles deployed under the canopy to track differences in biomass  
across transects, showing the relation of GNSS-based attenuation to lidar-based vegetation height (Ghosh et al., 2024, 2025).  
However, these GNSS-T configurations cannot be used to evaluate non-forested biomes with shorter statured vegetation, which  
encompass more than half of Earth's land surfaces. Instead, reflectometry GNSS configurations that evaluate the difference  
115 between the direct microwave signal received from satellite and the indirect microwave signal reflected from the surface  
provide an integrated estimate of both soil moisture and vegetation water content (Chen et al., 2016). Furthermore, the  
normalized microwave reflection index (NMRI) processes these signals to isolate the vegetation signal from the soil signal  
(Small et al. 2014). This approach therefore enables evaluation of vegetation water content of shorter statured vegetation  
(Larson and Small, 2014), which theoretically satellite VOD should be more suited to observe than dense forests (Chaparro et  
120 al., 2022). While GNSS-reflectometry approaches for vegetation monitoring have been conducted from satellites (CYGNSS)  
(Asgarimehr et al., 2024), GNSS interferometric reflectometry (GNSS-IR) can be conducted at site scales with a fixed sensor  
that measures the phase difference between the direct and surface-reflected signal (Larson, 2016). Such evaluation of these  
ecosystems can be critical for understanding, for example, cropland and rangeland forage yields and water stress, herbaceous  
vegetation fuel loads, as well as the role of grassland biomass in the carbon cycle (Allred et al., 2022; Sala. and Lauenroth,  
125 1982). GNSS-IR instruments have a legacy of use, but mainly for applications other than vegetation monitoring (Larson, 2016),  
and therefore could be an asset for more widespread use in the context of satellite VOD validation and plant hydraulics studies  
(Devine et al. 2026). These cross-scale remote sensing studies in heterogeneous dryland systems like the western U.S. are  
critical, and especially aligned with the NASA Adaptation and Response in Drylands (ARID) field campaign (Feldman et al.,  
2024).

130

Across the Western U.S., 1,100 GNSS-IR sensors were installed to evaluate plate deformation in a network called EarthScope  
Plate Boundary Observatory (PBO) (Larson and Small, 2014). Previous research demonstrates that grass and shrub vegetation  
water content can be monitored using the NMRI metric, which isolates soil moisture, soil properties (type, roughness), and  
topographic influences (Larson and Small, 2014). NMRI is available at these PBO sites. NMRI has been shown to directly  
135 relate to in-situ measurements of vegetation water content and vegetation height (Jones et al., 2014; Small et al., 2014; Zhang  
et al., 2017). Despite its physical difference from VOD, GNSS NMRI retrievals are likely the closest, most feasible and  
relatively cost-effective method (approximately 10k USD per sensor setup with newer options closer to 1k USD) to directly



capture the microwave signal from these shorter statured vegetation types across an approximately 100m scale. NMRI has been initially determined to represent a similar signature as satellite-based VOD to some degree (Jones et al., 2014; Zotta et al., 2024), and PBO NMRI has been used along with satellite measurements to create joint VWC products (Li and Sawada, 2022; Pan et al., 2020; Zotta et al., 2026). However, a more comprehensive comparison between GNSS NMRI and satellite-based VOD is needed across timescales, vegetation types, and microwave algorithms to evaluate its usefulness as a resource for calibration and validation. This is especially important for validating SMAP and SMOS based VOD as well as for upcoming multi-frequency Copernicus Imaging Microwave Radiometer (CIMR) measurements (Kilic et al., 2018). Such evaluations also serve as a precursor for comparisons between GNSS NMRI and higher spatial resolution vegetation water content retrievals from synthetic aperture radar (SAR) (i.e., NISAR, Sentinel-1) (Hajj et al., 2019).

Here we ask: do site-level microwave measurements with GNSS-based reflectometry show potential for validating and providing insights into satellite microwave vegetation retrievals? What factors impact correlations between site and satellite vegetation microwave measurements? We provide an initial assessment of GNSS-IR sites across the Western U.S. and investigate how GNSS NMRI and satellite VOD correlate across vegetation type, spatial heterogeneity of vegetation within the satellite footprint, microwave measurement frequency, and retrieval algorithm. We also evaluate differences across timescales including correlations at seasonal timescales, related to phenology, versus daily anomalies, related to response to rainfall events. Given that both satellite VOD and GNSS NMRI are error prone, we do not present either metric as closer to the true vegetation water content, as both of their capabilities of capturing true vegetation moisture and biomass dynamics are not yet known.

## 2. Methods

### 2.1 Datasets

Our main datasets for the analysis included GNSS-IR sites and satellite VOD products across a common April 2015 to December 2017 period when all data products are available. GNSS-IR sites are used from the PBO network, from which we used the NMRI metric that was produced as a part of the PBO H2O initiative to translate these signals to hydrologic variables (Larson, 2016; Larson and Small, 2014). While newer GNSS instruments measure all constellations, the PBO instruments only measure GPS constellation signals. Our study domain is the western U.S. in the coterminous U.S. where most PBO instruments are located (removing Alaska sites). There are ultimately 272 sites that have an NMRI time series in our study period and spatial domain. NMRI is a normalized metric computed via:

$$NMRI = -\frac{(MP_1rms - \max(MP_1rms))}{\max(MP_1rms)} \quad (1)$$

where  $MP_1rms$  represents vegetation structure and surface roughness from the downward reflected microwave signal incoming from GPS sensors at 1.5 GHz frequencies (L-band) (Larson and Small, 2014).  $MP_1$  stands for multipath pseudorange and rms refers to the root mean square of this signal. The 1 subscript refers to the L1 GPS sensors which measure at 1.5 GHz, which is



close to SMAP's 1.41GHz frequency.  $MP_{1rms}$  is derived from interference of the direct incoming GPS microwaves and weaker reflected microwaves, which is a function of vegetation attenuation and scattering (Larson, 2016). Lower  $MP_{1rms}$  relative to the maximum value indicates more vegetation extinction from water content presence.

175 We evaluated satellite passive microwave VOD products across L-band (1.4 GHz), C-band (6.7 GHz), and X-band (10.7 GHz),  
and across two different types of retrieval algorithms. Namely, we used the SMAP-based L-band VOD product from the multi-  
temporal dual channel algorithm (MT-DCA) at a 9km equal area scalable Earth 2 (EASE-2) grid scale (Feldman et al., 2021d;  
Konings et al., 2016). This MT-DCA algorithm simultaneously retrieves soil moisture and VOD, while using a regularization  
approach which stabilizes the retrieval and reduces algorithm-based retrieval errors (Ebtehaj and Bras, 2019; Gao et al., 2020;  
180 Konings et al., 2015). For comparison, we also used AMSR-2 VOD retrievals at C-band and X-band from the same MT-DCA  
algorithm, which uses SMAP soil moisture as an input (Baur et al., 2019). These retrievals are available at 36km resolution on  
the EASE2 grid. Finally, we obtained AMSR-2 VOD retrievals at C-band and X-band from the land parameter retrieval model  
(LPRM) algorithm and regridded them to 9km (de Jeu, 2013; Owe et al., 2008). The LPRM algorithm uses a more traditional  
approach of simultaneously retrieving soil moisture and VOD without a regularization process. We additionally upscaled the  
185 9km products to 36km to test the impact of the grid scale on the results. We note several additional differences between the  
VOD algorithms. A prominent source of differences between the VOD retrieval algorithms is how they handle land surface  
temperature inputs in using different sources from reanalysis (Zotta et al., 2026). Our use of AMSR-2 VOD from the MT-  
DCA and LPRM is sensitive to these temperature differences. Furthermore, AMSR-2 instrument measures at a 55-degree  
angle, whereas SMAP's incidence angle is 40 degrees. While these angles are already factored into the retrieved VOD values,  
190 AMSR-2's higher incidence angle likely make the microwave retrievals relatively more vegetation-sensitive than for SMAP.  
Finally, we use VOD from SMAP's 6:00 am local measurement time and AMSR-2 VOD from its 1:30 am local measurement  
times which these time differences are not anticipated to create substantial divergences between VOD outputs from overnight  
rehydration. In fact, the use of these nighttime/morning overpasses is to reduce uncertainties related to soil and canopy  
temperature inputs. Ultimately, the use of five different VOD products allows direct comparison across the different LPRM  
195 (traditional dual-channel approach) and MT-DCA (regularization approach) algorithms as well as across SMAP and AMSR-  
2 satellite instruments with different measurement frequencies (L, C, and X band).

We also used several auxiliary datasets. As an additional point of comparison with GNSS NMRI, we used satellite soil moisture  
from the SMAP MT-DCA retrievals (Feldman et al., 2021d). This product was used instead of the official SMAP L3 product  
200 because of known coupling of soil moisture errors with vegetation in the SMAP L3 product (Crow and Feldman, 2025; Dong  
et al., 2018). Therefore, the SMAP MT-DCA algorithm soil moisture is less likely to have a built-in, erroneous influence of  
VOD that might inflate relationships between soil moisture and VOD. We additionally used 30m resolution land cover data  
derived from Landsat during 2020 (Potapov et al., 2022). Vegetation type classifications were divided into short statured  
vegetation, dense short statured vegetation, cropland, and forest based on this data product's designations. Finally, we used



205 MODIS 16-day 500m NDVI to classify growing season timing and as an additional point of comparison in our seasonality analysis (see below) (Small et al., 2018).

## 2.2 Correlation Analysis

We computed the daily-scale Pearson's correlation between GNSS NMRI and VOD from each of the five VOD products and  
210 computed the percentage of sites with a positive, statistically significant ( $p < 0.05$ ) correlation. NMRI is reported daily while the VOD values are typically available approximately at least every three days. We therefore only used the data pairs on the days when both NMRI and VOD are available. We only evaluated the correlation between VOD and NMRI because these metrics are inherently different; it is not possible to compute meaningful root mean squared errors or absolute biases. The GNSS NMRI correlation with soil moisture was also computed. We subtracted the NMRI correlation with soil moisture from  
215 the NMRI correlation with each of the VOD products as a test of whether the microwave vegetation signal (within NMRI) is partitioned from the soil moisture signal.

These correlations were also binned based on vegetation types and the satellite pixel's spatial heterogeneity. To account for vegetation types, we used both the 30m scale vegetation type that the NMRI site is in as well as the dominant vegetation type (mode) of the satellite pixel that the GNSS site is contained within. To consider the satellite pixel scale spatial vegetation  
220 heterogeneity, we evaluated two different metrics. First, we computed the Shannon entropy of the percent coverage of each of the four land cover types via:

$$H(x) = -\sum_x p(x) \log_{10}(p(x)) \quad (2)$$

where  $p(x)$  is the distribution of four values of percent coverage of the vegetation types. The percent coverage of each land cover within a pixel is the amount of a 9km satellite pixel occupied by 30m resolution land cover types. Smaller values of  $H(x)$   
225 represent a scenario of mostly one land cover type, or more homogenous land cover, whereas higher values indicate higher heterogeneity with a spread of multiple land cover types within the satellite pixel. The second metric we evaluated is the percentage of the land cover within the satellite pixel that the GNSS sensor exists within, which we designated the site vegetation type pervasiveness. For example, if the GNSS sensor is located within an ecosystem dominated by short statured vegetation (based on the 30m resolution land cover data), the value for that site is the percent coverage of the short statured  
230 vegetation across the 9km pixel. Higher values of this site vegetation type pervasiveness indicate that the site is within the dominant land cover type seen by the satellite. We binned the correlations based on these two metrics to assess their dependence on land cover heterogeneity.

## 2.3 Seasonal and Daily Anomaly Timescale Analysis

235 The correlations were additionally evaluated at different timescales of daily-scale anomalies from the seasonal cycle (to capture co-variation of high frequency variability) and across the seasonal cycles only (lower frequency variability). To separate these two timescales, we first computed the mean seasonal cycle by averaging together days from different years into mean climatology (for example, the value of the 110<sup>th</sup> day of year is the mean of the values of the 110<sup>th</sup> day of year across 2015,



2016, and 2017). We only averaged together years 2015 to 2017 to remain with consistency across the datasets, though  
240 acknowledging a lower sample size to create the average seasonal cycle. To partly mitigate this lower sample size, the mean  
climatology was also then smoothed with a 30-day moving average window. This time series was considered the seasonal  
cycle with sub-monthly variability removed. To compute the daily-scale anomalies, we subtracted this seasonal average from  
the original time series to isolate sub-monthly variability. This analysis was carried out for NMRI and each of the satellite  
VOD products. Thereafter, we computed the NMRI correlation with each of the VOD products at each of these two timescales.  
245 As an additional assessment of the relative degree of seasonality compared to the daily-scale frequency variations of each  
vegetation microwave dataset, we computed the ratio of the standard deviation of the daily-scale anomalies to the seasonal  
amplitude of the seasonal cycle. The seasonal amplitude was computed as the 95<sup>th</sup> percentile minus 5<sup>th</sup> percentile of the seasonal  
cycle.

250 Next, we gave context to these correlations by evaluating more physically interpretable features of the seasonal timescales and  
the daily timescales. To further interpret the seasonal timescales, we compared the peak growing season timing of NMRI and  
satellite VOD products using two different seasonal timing metrics. The first metric used is the Julian day of year of the peak  
of the smoothed seasonal cycle (see Section 2.2). The day of year peak of NMRI at each site and the satellite VOD were  
subtracted to compare their timing. We also used a second metric less sensitive to the peak of the seasonal cycle: the timing of  
255 the maximum positive cross correlation between NMRI and each satellite VOD product. The 16-day NDVI time series was  
also evaluated as a reference.

To further interpret the daily-scale anomalies, we evaluated the response of NMRI and VOD to growing season rainfall pulse  
events, which are expected to be detectable in dryland regions like those in the Western U.S. (Feldman et al., 2021b). SMAP  
260 satellite soil moisture was used to identify rainfall events as an initial soil moisture increase (from previous overpass to the  
largest soil moisture peak before the drydown is initiated) followed by soil moisture drying over at least three consecutive  
SMAP overpasses (approximately 5-8 days). These surface soil moisture drydowns capture the wetting and drying associated  
with individual rainfall events, as demonstrated in previous studies (Akbar et al., 2018; McColl et al., 2017). Only above  
average soil moisture pulses were considered, which were estimated as the events where the initial increase of soil moisture is  
265 greater than the median of all events. Additionally, only soil moisture pulses during the growing season were considered in  
order to remove periods of no vegetation response (Collins et al., 2014). The timing of the growing season was approximated  
as the 180-day window around the peak NDVI determined in the above seasonality analysis. Our analysis does not appear  
sensitive to this definition. To normalize the VOD and NMRI responses across different sites and pulse events, the incremental  
rates of change per day were computed as:

$$270 \text{ NMRI Rate of Change} = \frac{NMRI_t - NMRI_{t_{previous}}}{t - t_{previous}} \frac{1}{NMRI_{t_{previous}}} \quad (3)$$



where  $t$  is the respective day after the pulse and  $t_{\text{previous}}$  is the day of the last available measurement. The normalization by  $\text{NMRI}_{\text{previous}}$  makes the quantity unitless and allows comparison of relative changes after pulses across sites and different rainfall pulses within sites. Equation 3 was analogously carried out for each VOD product. Finally, for each day after the pulse ends, the 25<sup>th</sup>, 50<sup>th</sup>, and 75<sup>th</sup> percentile rates of change were computed across all pulses and sites. As an example, a positive value on day 0 indicates that NMRI typically increases from before to after the rainfall pulse event. As a summary metric at each site, we computed the percentage of rainfall pulses for which NMRI increases on day 0 of the pulse, which indicates how frequently NMRI increases after a given rainfall pulse event. The median magnitude of these post rainfall responses was computed as well. The same metrics were computed for comparison with the satellite VOD products.

## 280 2.4 Attribution Analysis

Linear and random forest regressions were carried out to attribute spatial variations in VOD-NMRI correlations as well as differences in these correlations across the VOD products. The VOD-NMRI correlations were related to several potential controlling variables across space. This includes the two land cover heterogeneity metrics (Section 2.2) and vegetation type information from tree cover (percent of 30m tree cover pixels within the satellite pixel), both of which are expected to reduce the correlations. Mean climatic information was captured via mean annual soil moisture and mean NMRI, which serves as a proxy for average vegetation moisture amount. Vegetation seasonality was evaluated with the NMRI amplitude which is computed as the difference between the 95<sup>th</sup> and 5<sup>th</sup> percentiles of the NMRI smoothed climatology time series and normalized by the NMRI mean. Finally, the daily-scale variations were evaluated via the standard deviation of the VOD and NMRI anomaly time series. We refer to these variables as attribution factors.

To evaluate differences in the correlations for different VOD measurement frequencies, we subtracted the correlations between SMAP L-band MT-DCA VOD and NMRI and AMSR-2 MT-DCA X-band VOD and NMRI. These correlation differences were then linearly regressed against each of the potential attribution factors. Statistically significant correlations ( $p < 0.05$ ) suggest a given factor drives a closer relation of VOD at a given frequency to NMRI. To evaluate the effects of different VOD retrieval algorithms, this same procedure was also carried out for the difference in correlations between AMSR-2 X-band MT-DCA VOD and NMRI and AMSR-2 X-band LPRM VOD and NMRI.

To evaluate the relative impacts of these attribution variables on VOD-NMRI correlations, we carried out both multiple linear regressions and random forest machine learning regressions (RandomForestRegressor function from the Scikit-learn package in Python). Specifically, attribution factors were regressed against each of the VOD data products' respective correlations with NMRI. Variances explained of attribution factors were grouped based on land cover, land cover heterogeneity, mean climate (soil moisture), satellite VOD anomaly standard deviation (with the seasonal cycle removed), and GNSS-IR based seasonal amplitudes. Use of both techniques provides insights into confidence in estimated partial sensitivities of correlations to the attribution factors (e.g., considering linear versus non-linear relations).



305

Finally, for those attribution factors with significant relationships, we evaluated the increase in correlations between VOD and NMRI for only the sites with higher (>50<sup>th</sup> percentile) or lower (<50<sup>th</sup> percentile) values of the attribution variable (depending on which direction results in increases to the correlation). This binning is expected to capture the highest and lowest potential correlations.

310

### 3. Results and Discussion

#### 3.1 Overall site-satellite correlation patterns

Correlations between the site-based GNSS NMRI and satellite-based VOD products are significantly ( $p < 0.05$ ) positively correlated across 54% to 83% of the 272 considered Western U.S. sites (depending on the VOD data product) (Fig. 1). Daily-scale correlations range from 0 to 0.6, with a median of 0.14 at L-band to 0.41 with the X-band LPRM algorithm. The X-band VOD products have higher correlations with GNSS NMRI compared to lower frequency L and C band VOD. The LPRM products also tend to have higher correlations than MT-DCA algorithms (Fig. 1). While initially appearing low, these VOD-NMRI correlations are consistently higher than when correlating NMRI with the commonly used SMAP L3 satellite soil moisture (median of 0.02) (Figs. 1, S1). This suggests NMRI and VOD are capturing microwave vegetation signals more than soil signals; if NMRI represented soil moisture signals more, the correlations between NMRI and soil moisture will be higher than NMRI correlations with VOD. For NMRI-VOD correlations to be higher than NMRI-soil moisture correlations, the satellite VOD signal needs to be partitioned from the soil moisture signal and the GNSS NMRI value needs to partition the microwave vegetation signal more than the soil moisture signal (acknowledging both the VOD and NMRI signal will have some relation to soil moisture).

325

By contrast, analogous correlations between satellite and site level soil moisture, using the SMAP core calibration/validation sites as an example, are typically greater than 0.5 and can be as high as 0.95 (Chan et al. 2016, Colliander et al. 2017). However, there are several notable differences that should, in all cases, lead to lower correlations between VOD and GNSS NMRI. Core calibration validation sites have many distributed soil moisture sensors across the satellite pixel to capture spatial heterogeneity across the pixel (Colliander et al., 2019), whereas the GNSS comparisons here have typically only one site within the satellite pixel scale (see Section 3.3 for the few exceptions). Additionally, the site-level and satellite soil moisture are capturing the same metric whereas the VOD and NMRI indices are capturing vegetation attenuation in two different ways. Satellite VOD is capturing all vegetation attenuation of upwelling surface emission, while NMRI is capturing vegetation attenuation of incoming signals from satellites that observe only a fraction of the canopy per satellite overpass (Humphrey and Frankenberg, 2023). Finally, satellite soil moisture retrieval algorithms have been calibrated considering these site-level measurements, which will inherently improve the correlation, while VOD algorithms are largely uncalibrated to in-situ information. Therefore, lower correlations between VOD and NMRI are expected.

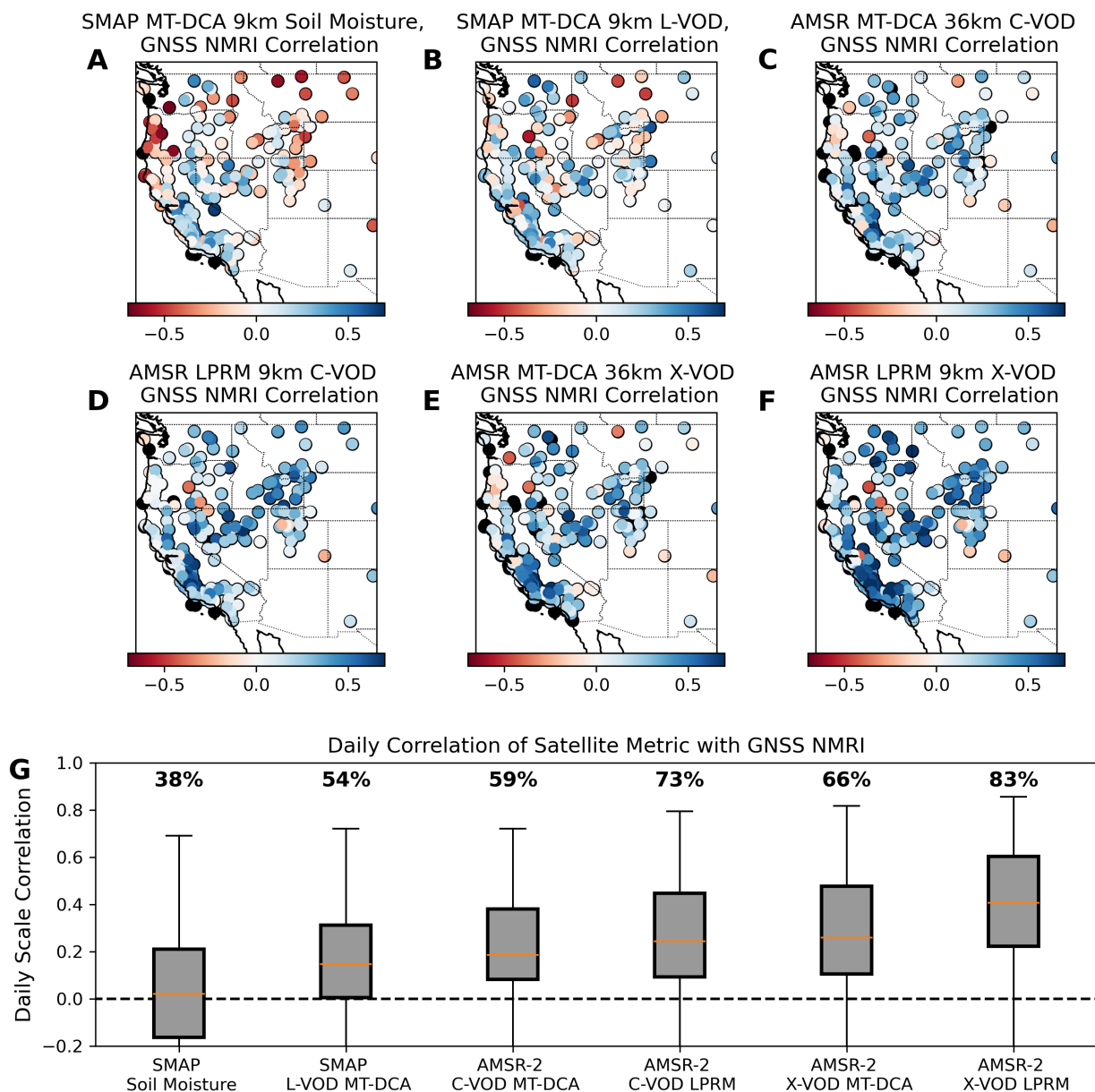
335



340 The results remain nearly identical when upscaling the 9km products to 36km to keep a consistent 36km grid scale across all products. For example, the correlations between the LPRM 9km correlation with NMRI are consistently similar (median correlation difference across sites of 0.004) to those when using LPRM 36km upscaled, for both C-band and X-band. This is expected because the radiometer resolutions are 30-40km for these sensors and the enhanced resolution from the Backus Gilbert interpolation only provides marginally finer resolution despite gridding at 9km (Chaubell et al., 2016). We choose to remain with 9km and 36km products because we wish to show results at the products' original gridding.

345

Spatial variability of correlations across the data products is apparent in Figure 1a-1f as well as in the distributions represented in Fig. 1g. Hereafter, we evaluate sources of variability in these correlations and, in particular, evaluate those that act to reduce the correlations. We investigate impacts of vegetation type, surface heterogeneity impacts due to differences in the GNSS footprint (tens of meters) and the satellite VOD footprint (tens of kilometers), measurement frequency differences, and 350 influences of physical processes at different timescales.



355 **Figure 1.** Daily scale correlations between site-based GNSS NMRI and respective satellite VOD products shown spatially across (a) SMAP L-band soil moisture (9km scale), (b) SMAP L-band MT-DCA VOD (9km scale), (c) AMSR-2 C-band MT-DCA VOD (36km scale), (d) AMSR-2 C-band LPRM VOD (9km scale), (e) AMSR-2 X-band MT-DCA VOD (36km scale), and (f) AMSR-2 X-band LPRM VOD (9km scale). (g) The spatial distributions of the respective variable and GNSS NMRI sites are also shown in boxplots for each map, with percentages above boxplots representing the percentage of correlations that are both positive and statistically significant ( $p < 0.05$ ). The SMAP soil moisture-based correlations are statistically significantly ( $p < 0.05$ ) lower than that of all of the VOD products based on Mann-Whitney U tests.

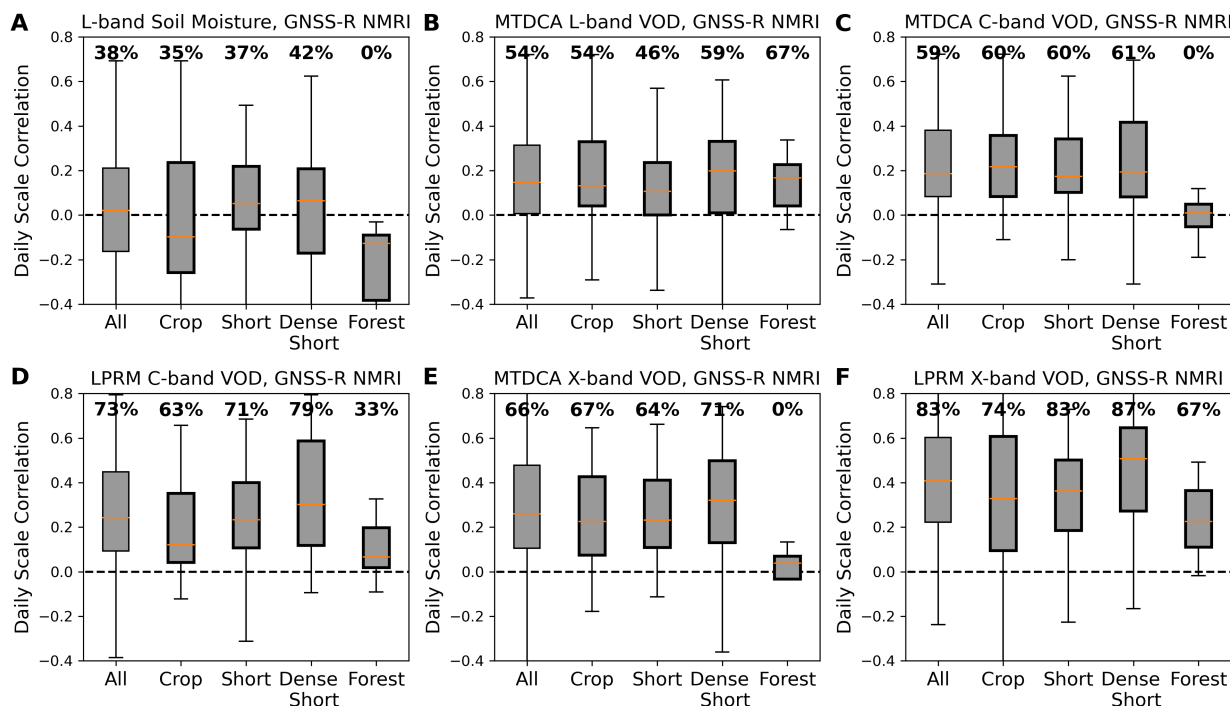


### 360 3.2 Site and Pixel-Level Vegetation Type Differences

Across most conditions, correlations between GNSS NMRI and satellite VOD are higher for shorter statured vegetation and crops than for sites nearby forests or within satellite pixels with higher forest cover (Figs. 2, S2). This is especially the case for C-band and X-band VOD products. By contrast, the correlations are similar across vegetation types at L-band. While Fig. 2 presents vegetation type binned based on the 30m land cover product, similar patterns are shown when considering the  
365 dominant land cover across the 9km satellite pixel that contains the GNSS site (Fig. S2).

There are several potential reasons for these patterns, especially for the lower correlations in forests at C-band and X-band. First, VOD will tend to have higher noise and variability in more forested pixels because the wavelength is often smaller than canopy constituents and thus will have more influence of multiple scattering from larger canopy structural features at the  
370 satellite pixel scale (Kurum et al. 2011). This will reduce the satellite-based VOD comparison with a field-based GNSS site. This scenario could be exacerbated where the GNSS site is located in a non-forested area, but also exists within a satellite pixel that contains a heterogeneous mixture of forests. Here, C and X-band VOD will have larger errors given the smaller wavelength of less than 5 cm. Similar correlations across vegetation types for L-band VOD also support this point given that L-band VOD is less likely to be sensitive to different mixtures of vegetation types in being more capable of sensing the depth of the forest  
375 canopies in this region; the longer L-band VOD wavelength (~21cm) is less sensitive to scattering and absorption for denser canopies than for C- and X-band (Baur et al., 2019). Second, there might be smaller differences of correlations across the vegetation types as well as smaller correlations for L-band VOD overall because the VOD product is capturing more of the soil signal than C and X-band VOD products. Third, the GNSS sites with taller vegetation in their vicinity will have an influence of higher biomass and attenuation (when the signal initially traverses downward through the canopy before surface  
380 reflection) that may add more noise to the GNSS NMRI signal. However, this case is likely not a common issue given that GNSS sites were placed in mainly open areas away from collections of trees (Larson and Small, 2014).

Ultimately, the fact that correlations are highest across a range of herbaceous vegetation types is consistent with expectations of the microwaves being able to penetrate smaller canopy features (with wavelengths of 2-21cm).



385

**Figure 2. Daily scale correlations between GNSS NMRI and the respective satellite VOD products across different land cover types, with the same format as Figure 1G. The land cover types here refer to that of the GNSS sites, determined from the 30m resolution land cover type product. The same figure is shown considering the dominant land cover type across the 9km satellite pixel that contains the GNSS sensor (Fig. S2). Percentages above boxplots represent the percentage of correlations that are both positive and statistically significant ( $p < 0.05$ ).**

390

### 3.3 Within-satellite pixel land cover heterogeneity

We investigate how the correlations are influenced by the spatial scale mismatch of GNSS NMRI sites (~100m scales) and the satellite footprints (~30 km scales) (Fig. 3). At sites with lower spatial vegetation variability, we find that correlations increase (generally by 0.05 to 0.1) and are more commonly significant and positive. VOD correlations are highest in 9km pixels with lower Shannon entropy of land cover types (low land cover type variability within the satellite pixel in Fig. 3). Additionally, they are higher when the GNSS site is located within that pixel's most dominant land cover type; the "site vegetation type pervasiveness" metric designation in Fig. 3 isolates the sites where the GNSS sensor is located within that pixel's dominant land cover. Taking the X-band VOD (from MT-DCA algorithm) as an example, the GNSS NMRI-VOD correlation can increase by more than 0.1 from the pixels with the highest to lowest spatial heterogeneity (Figs. 3B, 3C). Across most VOD datasets, this NMRI-VOD correlation significantly ( $p < 0.05$ ) decreases with higher vegetation heterogeneity and increases with higher site vegetation type pervasiveness, respectively (Figs. 3B, 3C). These results contrast with Jones et al. (2014) which found that surface heterogeneity did not show an influence on the AMSR-E VOD and NMRI correlations. This could

395

400



405 potentially be due to our use of a higher spatial resolution land cover data product (Landsat 30m instead of MODIS 250m) to estimate the spatial heterogeneity metric.

We additionally evaluate the six pixels (at 9km) that contain multiple PBO H2O sites. We find that averaging NMRI across the sites does, on average, result in marginally higher correlations with satellite VOD than the correlations of VOD with individual GNSS-IR sites (Fig. S3). However, there are still sites within the pixel that individually have higher NMRI correlations with satellite VOD than the pixel-average NMRI. This may be because these sites represent vegetation conditions that are more representative of the satellite pixel-scale conditions than other sites are. Ultimately, it is challenging to draw generalizable conclusions since there are so few satellite pixels with more than one GNSS-IR site, only a maximum of four sites within a given pixel, and only marginal improvements on average in correlations with VOD when averaging across the sites. However, this analysis does suggest that there is a potential to increase NMRI correlations with satellite VOD by placing multiple GNSS-IR sites across a pixel to represent sub-pixel heterogeneity, as well as allow investigations into why some sites individually have lower correlations.

410  
415

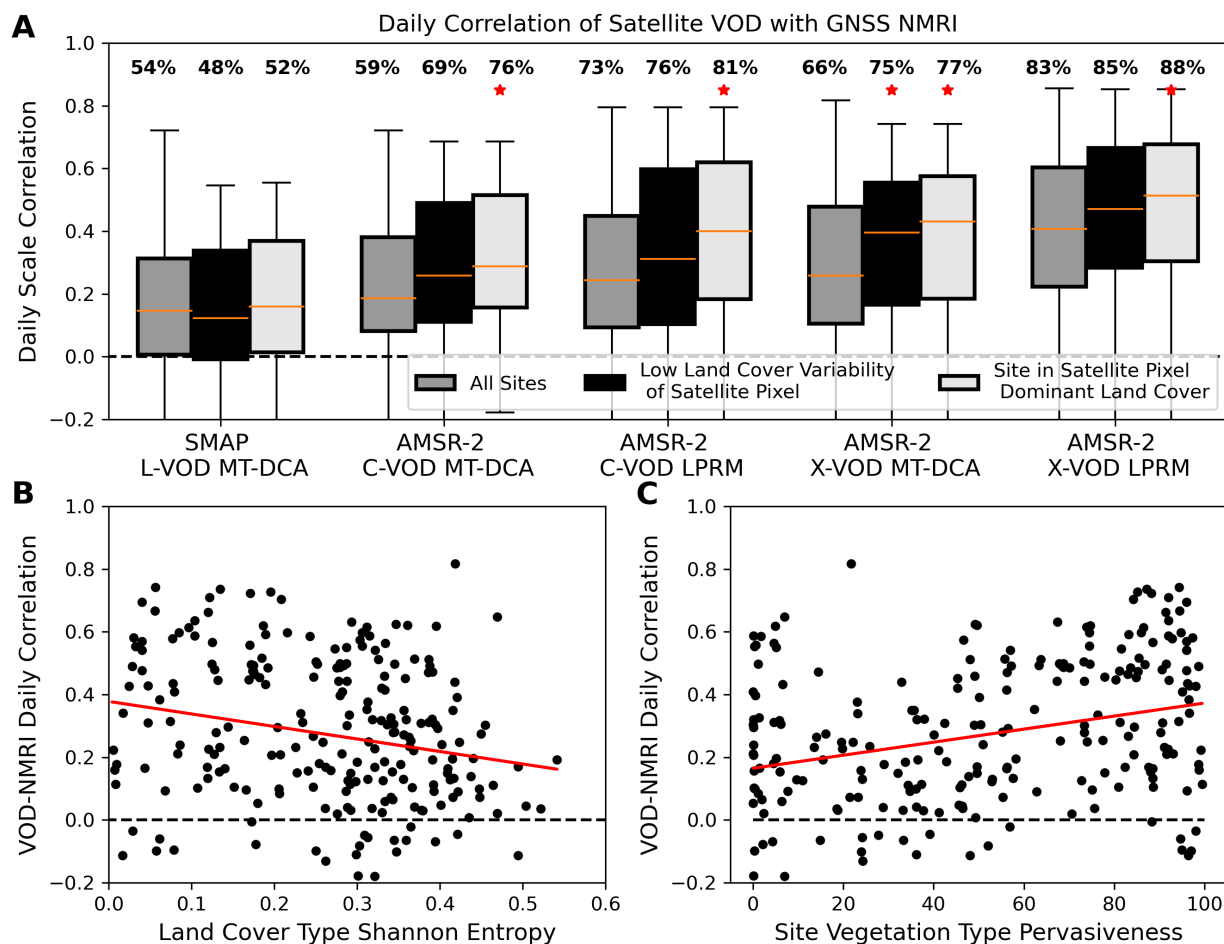


Figure 3. (A) Daily-scale correlations between GNSS NMRI site and respective satellite VOD products. All sites are shown alongside correlation distributions in the satellite pixels with the lowest land cover variability (<25<sup>th</sup> percentile Shannon entropy) and for GNSS sites with higher site vegetation type pervasiveness, or where the vegetation type at the GNSS site is the most dominant land cover across the 9km satellite pixel (>75<sup>th</sup> site vegetation type pervasiveness). Percentages above the distributions are the percentage of sites with a positive, statistically significant correlation ( $p < 0.05$ ). The asterisks above the boxplot mean that the that respective distribution has correlations statistically significantly ( $p < 0.05$ ) greater than the “All Sites” boxplot using Mann-Whitney U tests for differences of medians. (B) Correlations across different levels of Shannon entropy of land cover types shown in the example of GNSS NMRI correlations with X-Band VOD from AMSR-2 MT-DCA. (C) Correlations across site vegetation type pervasiveness. Higher values indicate that the GNSS site is within the satellite pixel’s most dominant land cover type. Like panel B, this considers GNSS NMRI correlations with AMSR-2 MT-DCA-based X-Band VOD. In both panels B and C, the values are significantly decreasing and increasing, respectively, based on linear regressions using the raw data pairs ( $p < 0.05$ ; red line represents the linear regression model fit of the data). These correlations are statistically significant for all other VOD datasets except for L-Band VOD and for panel C of AMSR-2 LPRM X-band VOD.



### 3.4 Measurement Frequency Differences

X-band VOD correlations with NMRI tend to be higher than correlations of NMRI with VOD at lower frequencies (Fig. 1). We evaluate the difference of L-band and X-band VOD correlations with NMRI here, where L-band VOD's correlation with  
435 GNSS NMRI is consistently lower than respective correlations of NMRI with higher frequency X-band VOD measurements (Fig. 4). This occurs both considering X-band VOD and L-band VOD retrieved using the same MT-DCA algorithm (Fig. 4A), as well as considering the X-band VOD from the LPRM algorithm (Fig. 4B). Figure 4 shows that the lower L-band VOD correlation with NMRI is relatively common, across 75% of sites when compared to MT-DCA X-band VOD and across 86% of sites when compared to LPRM X-band VOD. Correlations with L-band VOD being lower than those with X-band VOD of  
440 both products suggest this is also not due only to algorithmic differences. Nevertheless, the larger X-band correlations are surprising considering NMRI is based on the L-band GNSS satellite signal, and thus in theory NMRI should relate more closely to L-band VOD. Such a result is not unique to SMAP or the MT-DCA algorithm since lower correlations with NMRI were also found for a different L-band VOD product that integrates L-band measurements from SMAP as well as Soil Moisture and Ocean Salinity (SMOS) satellites (Zotta et al. 2014).

445

In the typically less densely vegetated biomes of the Western U.S., it is possible that X-band VOD can have an improved representation of field-based microwave vegetation signals. The annual mean X-band and L-band VOD are highly correlated ( $r = 0.73$  across the sites) with no indication of saturation at X-band, suggesting that X-band VOD is at least as suitable for observing a biomass signal similarly to the biomass signal as L-band in short-statured vegetation (Olivares-Cabello et al.,  
450 2023). Furthermore, several factors appear to be associated with higher X-band VOD correlations with GNSS sites relative to those of L-band, including lower spatial heterogeneity, lower tree cover, drier soils, higher mean NMRI, and larger NMRI seasonal amplitude (Figs. 4C, 4D). Notably, X-band VOD has closer relationships with GNSS NMRI variations in drier environments with less tree cover, suggesting that X-band VOD is potentially better representing the typically less dense vegetation in these mostly dry environments (Fig. 4C, 4D). In principle, these smaller statured vegetation types may cause  
455 similar attenuation between X-band and L-band signals. X-band VOD has lower correlations with NMRI in forested locations, especially relative to L-band, which supports this idea. Two potential error sources reduce VOD and NMRI correlations in forested pixels. Importantly, more forest cover in a pixel will result in more multiple scattering and more error retrieving VOD (Kurum et al., 2011), and especially at higher frequencies. Furthermore, NMRI is potentially reduced in its comparison to VOD when the sites are nearby forested areas because the NMRI signal becomes more dependent on the pathways of incoming  
460 GNSS signals that might initially travel through taller vegetation structures before being reflected from the ground. This is contrast to VOD observing all directions of upwelling emission across canopy geometries. Finally, larger seasonal amplitudes of NMRI may also relate to larger X-band VOD relations with NMRI, suggesting that X-VOD more closely resembles the seasonal cycle of NMRI and/or that NMRI is highly sensitive to the seasonality of the vegetation structure than observed with L-band VOD.

465



470 The fact that L-band VOD correlations are similar across vegetation types and land cover heterogeneity is consistent with the expectation of being less prone to signal saturation in denser canopies than higher frequencies; the L-band VOD signal is less influenced by variations in vegetation types across the pixel. By contrast, X-band VOD increases its correlations with GNSS NMRI under lower spatial heterogeneity of vegetation types within a pixel (Fig. 4); the X-band signal across the pixel scale may be relatively more influenced by vegetation scattering of smaller leaves and branches and thus responds more to the sub-pixel vegetation heterogeneity than L-band VOD.

475 Another potential reason for lower L-band VOD correlations with NMRI is that the L-band emission across the satellite pixel is likely relatively more sensitive to soil moisture than C-band and X-band emission, especially in these less vegetated environments and under drier soils (Fig. 4). Indeed, under dry soil conditions, the L-band emission originates from deeper soil layers which should increase the relative sensitivity of the L-band emission to soil moisture over the vegetation signal (Moghaddam et al., 2000). Analogously, site level experiments with L-band versus even longer-wavelength P-band shows that P-band emission loses sensitivity to the vegetation signal and gains sensitivity to soil moisture (Shen et al., 2024). Longer wavelengths could thus create more uncertainty retrieving VOD at these sites that have less dense vegetation.

480

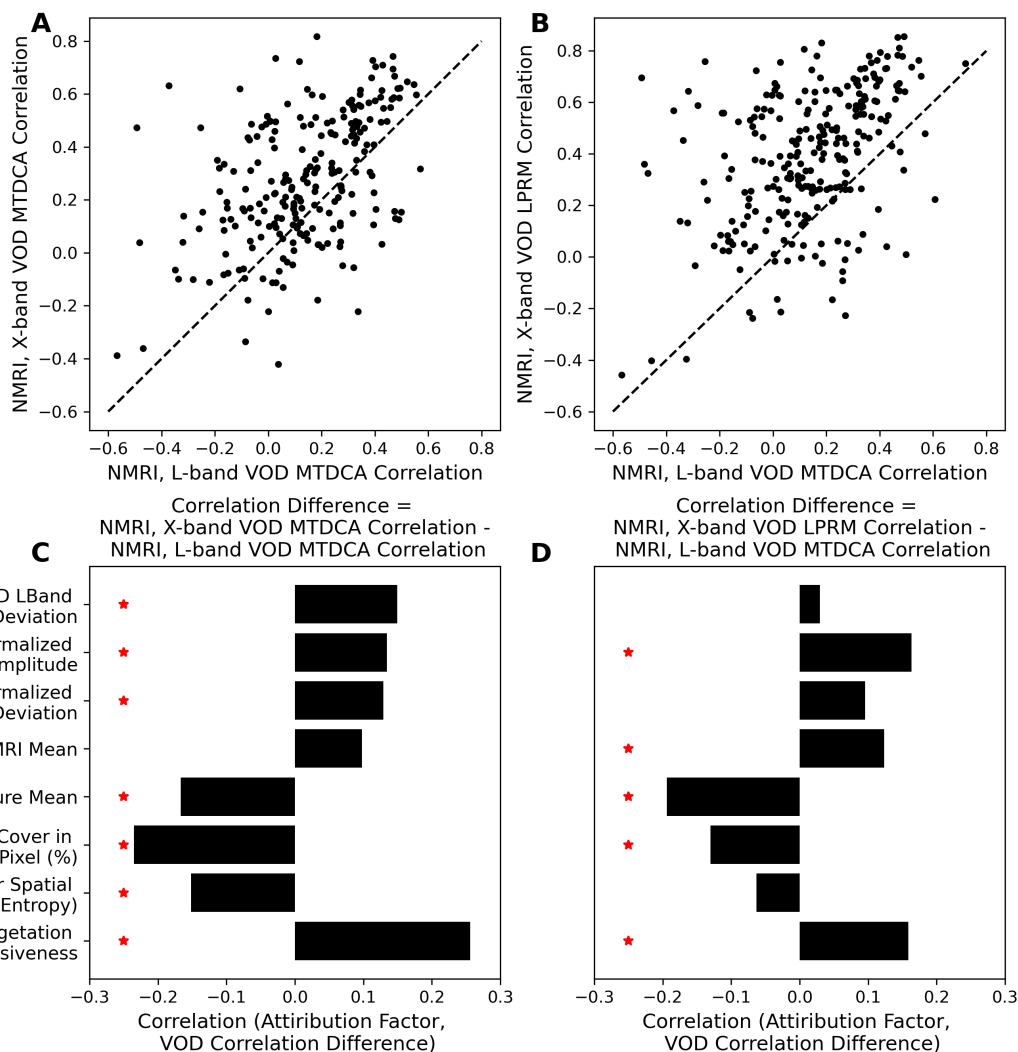


**Figure 4.** Comparison of correlations between L-band VOD with GNSS NMRI with the correlations of NMRI with (A) X-band VOD from the MT-DCA algorithm and (B) X-band VOD from the LPRM algorithm, where each symbol represents one site. Values above the 1-1 line indicate that the X-band VOD product has a higher correlation with NMRI than L-band VOD does for that site. (C) Relations between attribution factors and the difference of correlations between NMRI with X-band MT-DCA VOD and NMRI with L-band MT-DCA VOD (difference of y and x-axis values in panel (A)). (D) Same as Panel (C) but difference of correlations between NMRI with X-band LPRM VOD and NMRI with L-band MT-DCA VOD (difference of y and x-axis values in panel (B)). Scatter plots of these relationships are shown in Fig. S4 for the X-band LPRM algorithm (panel D) as an example.

### 490 3.5 Timescale Differences: Seasonality Versus Daily Scale Anomalies

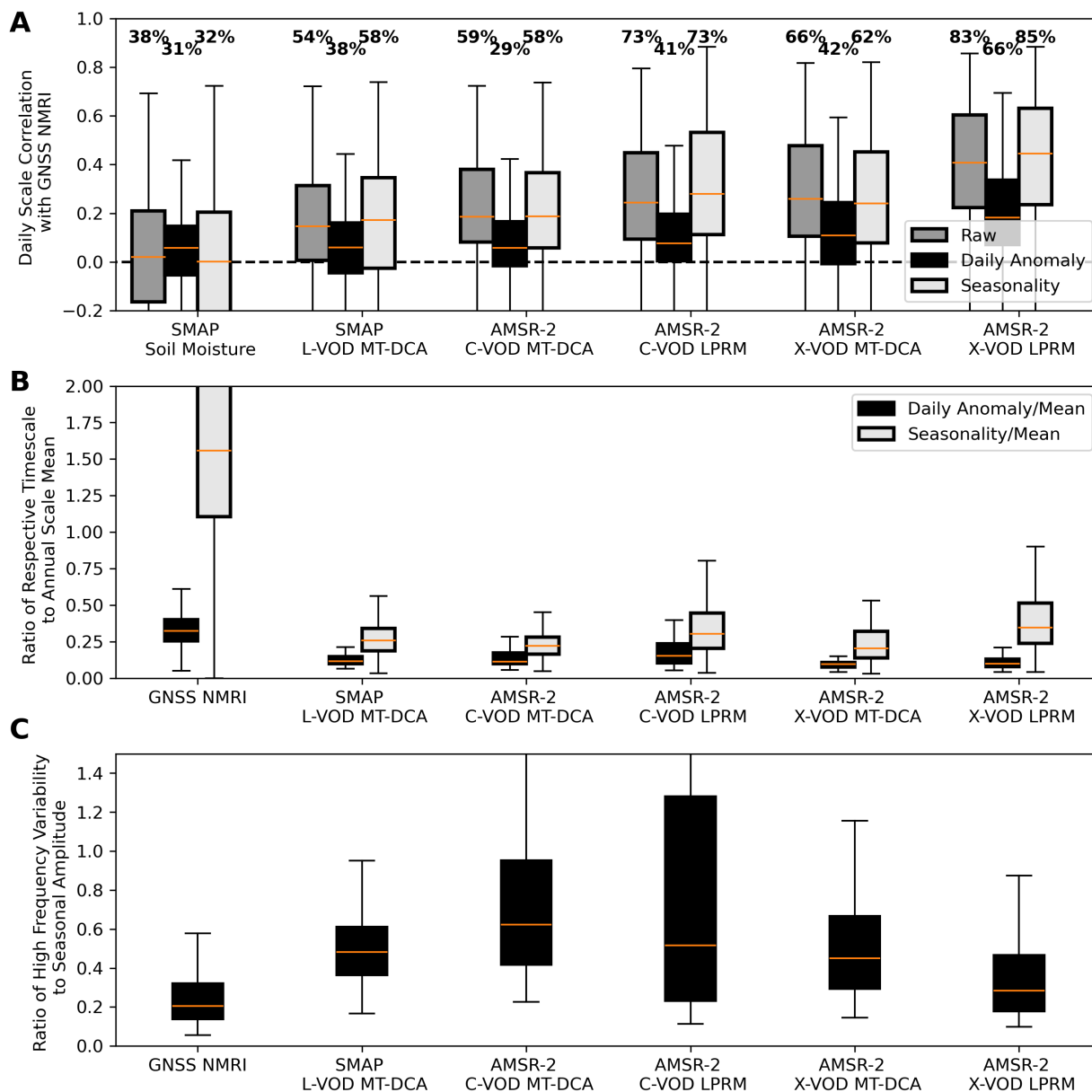
To provide additional context and attribution for our results, we also analyzed differences in GNSS NMRI-satellite VOD correlations for seasonal cycles (with daily scale anomalies removed) and daily-scale anomalies (with seasonal cycles



removed) (Fig. 5A). Across all VOD products, VOD and NMRI have higher seasonal cycle correlations compared to daily-scale anomaly correlations. Such an increase of associations between seasonal cycles compared to other timescales is expected across many geophysical variables and can be due to a common climatic forcing (i.e. incoming solar radiation) rather than causal relations between the variables (Tuttle and Salvucci, 2017). Additionally, the process of isolating the seasonal cycle removes high frequency noise sources, which inherently increases seasonal-scale correlations. By contrast, correlations for daily-scale anomalies will be inherently lower because common seasonal scale forcing in the time series is removed and high frequency noise sources remain. As another source of higher seasonal-scale correlations, NMRI has a substantial seasonal amplitude relative to its mean (Fig. 5B) and relative to its high frequency variations (Fig. 5C). The satellite-based VOD products by contrast have relatively larger high frequency variations.

As an initial insight from this partitioning, an increased correlation for NMRI with X-band VOD (Fig. 1) is likely related to X-band VOD's ability to track more features of the NMRI seasonal cycle relative to C-band and L-band VOD (Fig. 5). A larger seasonal amplitude increases the X-band VOD correlation with NMRI relative to the correlation with L-band VOD (Fig. 5). One potential reason is that, like X-band VOD, GNSS NMRI may have a relatively higher sensitivity to the biomass and structure signals, as evidenced in X-band VOD's and NMRI's relatively low daily scale variability compared to their seasonal amplitudes (Fig. 5B). Such strong relative relation of X-band VOD to biomass has been estimated previously (Zhang et al., 2019).

Ultimately, the partitioning of these timescales allows attribution of physically based sources of differences in the correlations, namely seasonal timing and rainfall pulse response of VOD and NMRI. We explore these points respectively in Sections 3.5.1 and 3.5.2.



515 **Figure 5. (A) Daily scale correlations decomposed into correlations between GNSS NMRI and satellite VOD for their daily scale anomalies only (high frequency variability) and seasonal cycles only (low frequency variability). (B) Ratio of the respective metric's high frequency variability and seasonal amplitude to annual scale mean. (C) Ratio of the respective metric's high frequency variability to its seasonal amplitude. Lower values, especially below 1, indicate the seasonal variations are relatively larger than the metric's high frequency variability.**

520

### 3.5.1 Seasonal Timing and Phenology



The seasonal peak timing of VOD from all products typically occurs within 30 days before NMRI (Fig. 6). VOD therefore compares more closely to the seasonal timing of GNSS NMRI than soil moisture which peaks 50-100 days before NMRI. Additionally, the seasonal timing of NMRI is typically closer to VOD than NDVI, with similar lags between these variables captured previously (Evans et al., 2014; Wang et al., 2020). These findings suggest that NMRI and VOD are detecting similar temporal vegetation features including their biomass and relative water content, rather than only moisture sources or only upper canopy functioning (greenness, photosynthetic functioning). The seasonal peak of VOD is nonetheless earlier than that of NMRI, which is consistent with a seasonality analysis by Jones et al. (2014). While that study suggested that the earlier seasonal peak of VOD was due to differences capturing scattering from smaller leaf and branch elements (due to their use of X-band instead of L-band VOD), we instead find a similar timing of seasonality of L-band VOD. Therefore, this difference may be due to VOD and NMRI physical representation differences rather than differences in measurement frequencies.

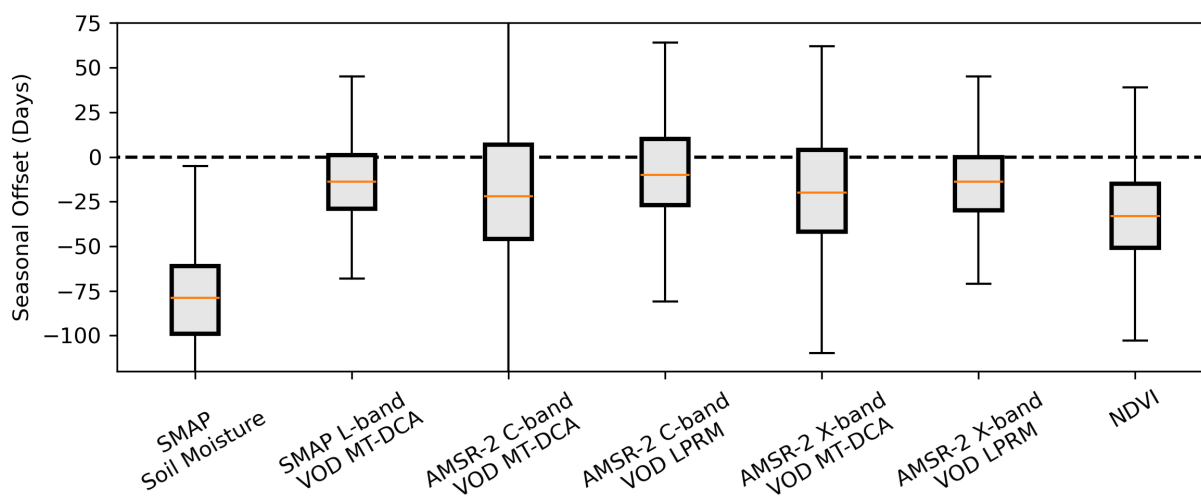


**Figure 6. Difference of NMRI seasonal peak timing with respective satellite-based metric across the available GNSS sites. The peak timing refers to the difference of NMRI seasonal cycle peak with that of the respective metric. All VOD-based products have statistically significantly smaller seasonal offsets than NDVI and soil moisture, based on Mann-Whitney U tests ( $p < 0.05$ ). A similar plot is shown using cross correlations in Fig. S5. Negative values mean that the respective product peaks before the NMRI seasonal peak.**

### 3.5.2 Daily Scale Rainfall Pulse Response

At daily timescales, microwave vegetation metrics are known to be sensitive to rehydration and growth following rainfall events (Feldman et al., 2021c)(Anoop et al., 2024). These can occur immediately and/or continuously in the several days following the rainfall pulse. During the growing season, the GNSS NMRI signal typically exhibits an initial increase immediately following the rainfall event (on day 0, which represents pre-pulse to during-pulse conditions), likely representing interception on the leaf surfaces and/or rehydration (Fig. 7A) (Schellenberg et al., 2024). This is followed by several days of

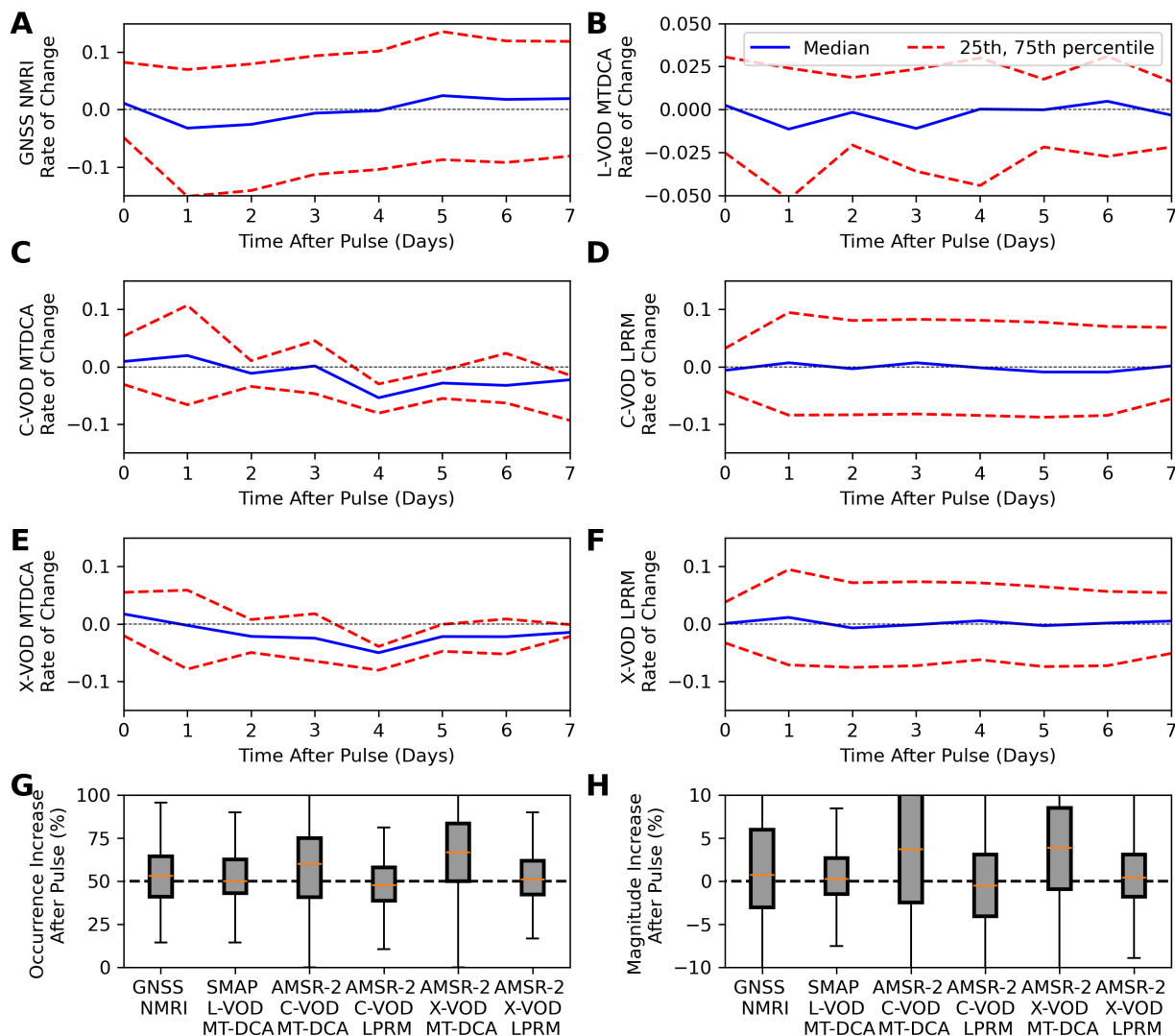


545 decreases likely due to plant drying during the ensuing dry spell. However, only the MT-DCA based VOD products (especially  
C and X-band, Figs. 7B, 7C, 7E) resemble this pattern with an initial increase followed by decreases. In fact, the C-band MT-  
DCA VOD product shows multi-day initial increases, while the other products rapidly switch to VOD decreases during drying  
one day after the rain event. The LPRM based C- and X-band VOD products mainly resemble noise at this timescale with  
nearly equal increases and decreases in VOD following the rain event with broad scatter. This difference in algorithms is  
550 expected because the MT-DCA uses a regularization method that reduces VOD noise especially at the sub-weekly scale  
(Ebtehaj and Bras, 2019; Feldman et al., 2021a). By contrast, the LPRM's simultaneous soil moisture-VOD retrieval approach  
is more susceptible to noise at these timescales (Dong et al., 2018), which appears to manifest as random fluctuations at sub-  
weekly timescales. Additionally, AMSR-2-based VOD is particularly susceptible to radio frequency interference in the U.S.  
(Zotta et al. 2024).

555

We further quantify how often VOD and NMRI increase the day immediately following the rainfall pulse, to test if rehydration  
and/or interception are detected (Fig. 7G). We find that the MT-DCA algorithms all have median values typically above 50%  
(L-band at 53%, C-band at 59%, X-band at 65%), while the LPRM algorithms exhibit values at or below 50% (C-band at 48%,  
X-band at 50%). The NMRI median is 53%, which compares more closely to the MT-DCA algorithm VOD products. Such a  
560 comparison is expected given some noise reduction due to regularization, which should act to increase this value whereas noise  
decreases it (Feldman et al. 2021).

However, while some of the VOD products analyzed appear to capture rainfall pulse responses, there is notably wide response  
variability (Figs. 7G, 7H). Since the daily scale rainfall pulse-drydown response is a component of the daily-scale anomalies,  
565 this range of responses to rainfall pulses and general mismatch between VOD and NMRI across the products partly explains  
why the daily-scale anomaly correlations between VOD and NMRI are low (Fig. 5A). These results may suggest that GNSS  
NMRI is relatively more suitable for evaluating seasonal changes in vegetation canopy structure and moisture changes rather  
than daily scale changes in relative water content levels, especially with VOD and NMRI showing more similar seasonal cycles  
than daily scale anomalies (Fig. 6). Additionally, NMRI may be capturing less daily scale variability of vegetation relative  
570 water content with its daily-scale variability relatively more subdued than satellite VOD (Fig. 5C). Some initial GNSS-  
transmissometry based results tend to support GNSS signals' lack of representation of internal water content compared to  
seasonal biomass variations (Burns et al., 2025). Potentially, the vegetation water content relationship with NMRI found at  
some PBO sites is more related to the seasonal rather than daily scale variations (Jones et al., 2014; Small et al., 2014).



575 **Figure 7. Responses of NMRI and VOD following rainfall events in the growing season. (A-F) Median rate of change responses**  
**following rainfall events in the growing season, as computed with Equation 3, where positive values indicate increases relative to the**  
**previous day. Results are shown for the median across sites as well as the 25<sup>th</sup> and 75<sup>th</sup> percentile. An increase on day zero, for**  
**example, indicates typical increases from before to the end of the rainfall. The dashed line is at values of zero for reference. Note the**  
**reduced y-axis limits in panel D given smaller relative MT-DCA L-band VOD variations. (G) Percentage of occurrences of increases**  
**following pulses on day 0 of the dry spell (immediately following the rainfall event). (H) The median magnitude of response of the**  
 580 **respective products in G. Positive values indicate more common increases of the metric immediately following rainfall events.**

### 3.6 Algorithmic Differences



X-band LPRM VOD correlations with NMRI are consistently higher than X-band MT-DCA VOD across 82% of sites (Fig. 8), which suggests that elements of the LPRM better represent NMRI in these ecosystems. This is considering that we upscaled the LPRM product to 36km (originally at 9km) to be consistent with that of the MT-DCA algorithm. The LPRM algorithm does have relatively lower correlations with NMRI compared to the MT-DCA at sites where VOD high frequency variability is higher (Fig. S6). This reduction is related to VOD errors when simultaneously retrieving soil moisture and VOD, which is partly mitigated within the MT-DCA (Feldman et al., 2021a), and manifests in less representation of the pulse responses seen in the NMRI signal (Fig. 7E, 7F). However, vegetation seasonality is dominating NMRI and VOD correlations (Figs. 5, 6), and therefore shows increased relationships with NMRI where the NMRI seasonal amplitude is larger (Fig. S7). The LPRM algorithm also appears to better represent NMRI in more heterogeneous and more forested sites (Fig. S6). Ultimately, the differences in correlation demonstrate that there are algorithmic-based differences in VOD detectable in this analysis; there may be a means to increase VOD correlations with GNSS NMRI solely by altering the retrieval algorithms. Therefore, GNSS-IR sites show value for calibrating VOD-based algorithms with initial efforts underway (Zotta et al., 2026). This is despite potentially large representativeness errors that may initially appear to limit GNSS-IR's utility for calibration and validation. As an example, shifts in the mean and variations of scattering albedo, land surface temperature, and surface roughness can substantially change the VOD time series (Baur et al., 2019; Feldman et al., 2018; Zhao et al., 2024), which suggests that these correlations can change substantially if altering these parameters. Thus, GNSS-IR sites may be used to calibrate these parameters and other VOD retrieval algorithm uncertainties.

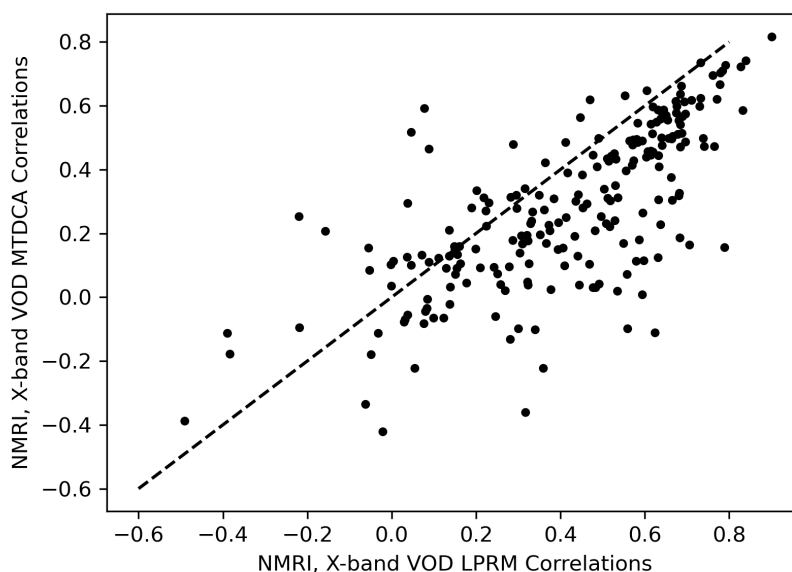


**Figure 8.** Comparison between the correlation of GNSS NMRI with X-band VOD from the MT-DCA algorithm and the correlation of GNSS NMRI with X-band VOD from the LPRM algorithm. Values below the 1-1 line indicate higher correlations of the LPRM algorithm with NMRI. Both VOD products are on a common 36km grid, removing effects of differences in resolution.



605

### 3.7 Potential Correlations

Based on the former analysis, we evaluate several potential factors and estimate their impacts on the correlations between satellite VOD and NMRI. These include spatial heterogeneity (the two metrics in Fig. 3), land cover (percent grass and tree cover), mean climate (mean soil moisture), high frequency VOD variations, and NMRI degree of seasonality. The microwave vegetation signal seasonality appears to be most important factor describing correlations, for both regression approaches and especially pronounced for the multiple linear regression approach (Fig. 9). Namely, these correlations tend to increase when the microwave vegetation signal contains a greater seasonal amplitude. However, other factors can increase the site-satellite correlations as well including drier moisture conditions and less tree cover (Fig. 9). The reported relative importances should be interpreted with caution considering the regressions often have total variances explained of less than 0.4, owing in part to regressing on uncertain correlation values. Additionally, the linear relationships appeared to be a best fit, whereas random forest regression methods had lower variances explained overall, suggesting that these relationships are best described as linear (Fig. S9). Nevertheless, statistically significant ( $p < 0.05$ ) correlations do exist between the site-satellite correlations and these individual factors suggesting that these factors all may play a direct role in altering connections between site and satellite vegetation microwave signals (Figs. 9b, S7, S8).

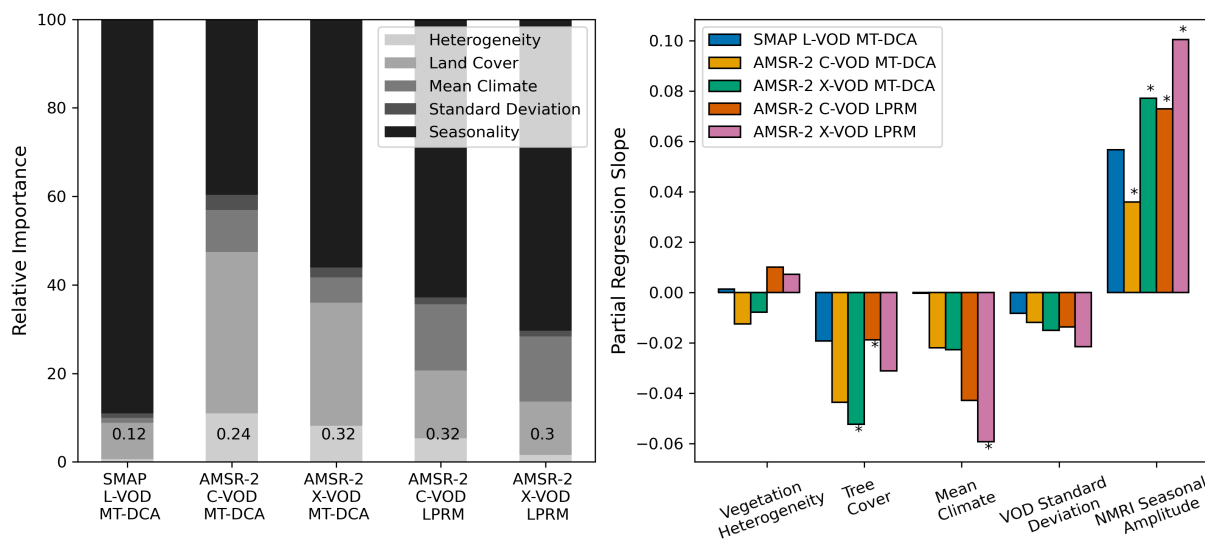
620

Overall, GNSS NMRI correlations with satellite VOD are generally higher in sites where there is low spatial vegetation heterogeneity, low forest cover, drier soil moisture, and larger seasonal NMRI amplitude (Figs. 9b, S7, S8). For the “highest potential” relations, we specifically bin sites that have greater than 50<sup>th</sup> percentile NMRI amplitude, less than 50<sup>th</sup> percentile soil moisture and tree cover across the western US, and only sites located in the dominant land cover type for that pixel (Fig. 10). 14% of sites meet these conditions and have correlations that are statistically significantly higher ( $p < 0.05$  from Kruskal-Wallis tests) than considering all sites together. In most cases, the C- and X-band VOD products have correlations with GNSS NMRI that are above 0.4 and often around 0.6. For the “lower potential” correlations, sites were selected with the opposite conditions to the “higher potential” correlations, which account for 8% of the sites. These sites have correlations that are statistically significantly lower ( $p < 0.05$  from Kruskal-Wallis tests) than both all sites and higher potential correlation sites. In nearly all cases, these correlations are below 0.2.

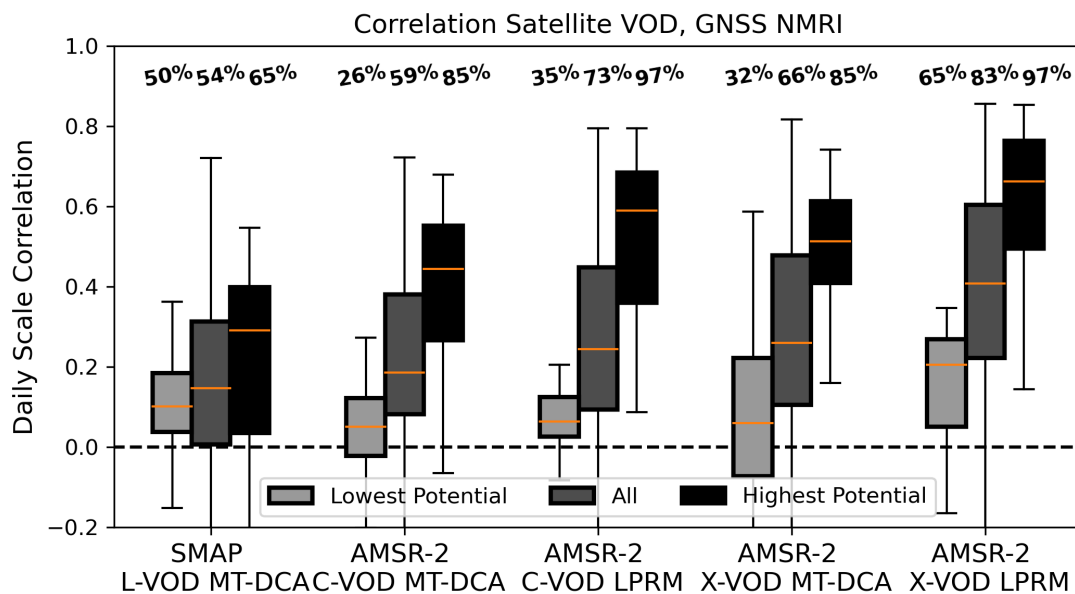
630

First, such an analysis demonstrates that there are physically explainable conditions for higher correlations in some sites, such that placement of GNSS sites matters for broader landscape representation of vegetation conditions and for satellite VOD validation. Second, the analysis may reveal an upper bound relationship between a single GNSS-IR site and satellite VOD retrieval over that site; this relationship is otherwise still limited to values near 0.6 due partly to the spatial scale mismatch and differences in representation of VOD and NMRI. Potentially, the relationship could still increase with the use of more sensors throughout the site. These sites under these criteria may also serve as the key sites selected for algorithmic calibration of satellite VOD products, under which calibration may serve to increase this relationship.

635



640 **Figure 9. (a) Relative feature importance of vegetation heterogeneity, land cover type (tree, grass cover), mean climate (soil**  
**moisture), standard deviation (satellite VOD), and seasonality (GNSS NMRI) for explaining the NMRI-VOD correlations using**  
**multiple linear regressions. Total variance explained is shown in text for each bar plot, which is used to normalize the partial**  
**variances explained (relative importance). Linear regressions are shown because random forest regressions tended to have lower**  
**variances explained (Fig. S9); this is likely due to linearity of the interactions and thus simpler linear models fitting the data. (b) The**  
645 **partial regression coefficients between individual factors and the respective NMRI-VOD correlations. Positive values indicate**  
**increases in that variable increase the correlations between NMRI and satellite VOD. Asterisks are noted above boxplots for**  
**statistically significant partial regression coefficients ( $p < 0.05$ ). Examples of individual linear regressions between explanatory factors**  
**and correlations between VOD and NMRI are shown in Figs. S7 and S8.**



650 **Figure 10.** The spatial distributions of the respective variable and GNSS NMRI sites, with percentages above boxplots representing the percentage of correlations that are both positive and statistically significant ( $p < 0.05$ ). Low versus high potential are sites binned based on all of the following criteria of high or low land cover heterogeneity in the pixel, higher or lower soil moisture, higher or lower tree cover, and lower or higher seasonal amplitudes, respectively.

#### 655 4. Conclusions

Correlations between GNSS NMRI and satellite VOD range between 0.2 and 0.6, showing some promise for GNSS NMRI to be used as a field-based method of observing water content of shorter statured vegetation canopies and a scalable means of validation of satellite VOD. However, while microwave GNSS-IR measurements and satellite VOD retrievals should observe the same vegetation canopy features (plant saturation and biomass), we find several site characteristics that tend to reduce these correlations. These include, but are not limited to, within-satellite pixel heterogeneity of land cover and wetter ecosystems with more tree cover. Therefore, these correlations tend to increase when GNSS sensors are placed in canopies that constitute the dominant land cover within the pixel, when the satellite pixel has more homogeneous land cover, and when drier and shorter statured, non-forested canopies are evaluated.

665 The correlations also further increase when using X-band VOD, especially from the LPRM algorithm, as well as when sites with larger seasonal cycles are considered. This result is unexpected given that GNSS-IR at the PBO H20 networks are measuring signals from L-band navigation satellites, and thus L-band VOD should theoretically have a closer comparison than X-band VOD with NMRI. However, unlike GNSS-T configurations, GNSS NMRI depends on the reflection of microwaves from the surface, which might increase the dependence of NMRI on the vegetation canopy structure, which VOD may be more



670 sensitive to at X-band than L-band. Additionally, several sources of evidence point to X-band and NMRI both more closely  
representing the seasonality of vegetation structure in these ecosystems dominated by shorter statured vegetation, compared  
to L-band VOD. First, the joint NMRI and X-band VOD correlations are highest considering only the correlations of their  
seasonal cycles and because the X-band correlations increase when the vegetation seasonal amplitude is larger. Both NMRI  
and X-band VOD also have relatively larger seasonal amplitudes relative to their daily-scale variations. L-band VOD, on the  
675 other hand, does not increase its relationship with NMRI in sites with higher NMRI seasonal amplitudes. L-band VOD might  
be relatively more sensitive to short-term variations in relative water content especially with the use of the MT-DCA algorithm  
that uses regularization to reduce noise at shorter timescale. NMRI nevertheless appears less sensitive to these shorter-term  
variations. Overall, our analysis suggests a lower sensitivity of L-band than X-band emission to seasonal variations in  
vegetation structure, especially for shorter statured canopies in the Western U.S.

680

Furthermore, satellite VOD correlations with site-level NMRI might be low because GNSS-IR evaluates individual path  
lengths of L-band signals through a canopy, which is physically different from upwelling emission measured by passive  
microwave radiometers across a 30km area from which VOD is derived. NMRI is also inherently a different metric from VOD;  
where VOD is the attenuation of microwave emission through the canopy, NMRI is a measure of roughness of the surface due  
685 to vegetation cover which may have a bias of sensitivity toward features of vegetation structure. In future work, VOD generated  
from SAR rather than passive radiometers (SMAP, AMSR, SMOS, etc.) might mitigate some of these differences in being  
similarly sensitive to microwave reflections from the surface and in having a higher spatial resolution. Finally, GNSS-IR are  
rotationally polarized while SMAP and AMSR-2 passive microwave radiometers are linearly polarized. The extent to which  
these electromagnetic considerations reduce the relationship between VOD and NMRI is currently not well known and needs  
690 to be further tested. Nevertheless, despite these differences, GNSS-IR appears to be a feasible, inexpensive method to obtain  
the field scale microwave vegetation signal from shorter statured vegetation.

Despite differences between field NMRI and satellite VOD, our results show promise that GNSS-IR sites can be used to  
monitor vegetation water content in spatially dominant grassland and shrubland ecosystems, whereas the increasingly  
695 implemented GNSS-T sites are mainly only able to evaluate tall-statured ecosystems (i.e., forests). When considering the most  
ideal site conditions to compare the satellite VOD to NMRI, correlations increase to a range between 0.3 to 0.7, suggesting  
that satellite VOD is feasibly resembling a microwave vegetation signal. These VOD-NMRI correlations are higher than with  
satellite soil moisture, suggesting that NMRI and satellite VOD are detecting a microwave vegetation and less so a soil moisture  
signal. If choosing X-band only, these correlations are typically above 0.6. By extension, this means that GNSS-IR sites can  
700 be used as calibration and validation tools for satellite VOD retrievals across different products, in the cases where these  
sensors are in more ideal conditions (“highest potential” cases in Figure 10). Such efforts are already underway for AMSR  
(Zotta et al. 2026), and by extension may be useful for calibrating VOD products from SMAP and SMOS as well as upcoming  
NISAR and CMIR. Operational VOD products have historically not been calibrated to in-situ vegetation information. Thus,



our findings point to a potential for improved VOD data products by using these sites as VOD calibration and validation  
705 opportunities in grassland and shrubland sites. In cases where NMRI and VOD do not closely relate, these provide further  
opportunities to understand causes of the mismatch to provide further insight into calibration and validation efforts.

We recommend further investigation of joint use of satellite VOD and GNSS-IR sensors, including installing several  
instruments within a satellite pixel to properly represent sub-pixel heterogeneity and capture the satellite-scale VOD signal.  
710 These sensors should be used in conjunction with GNSS-T sensors to represent grassland, savanna, and forested regions to  
both evaluate their vegetation water dynamics and validate satellite VOD. We also recommend GNSS-IR based studies along  
with site level instruments like dendrometers and psychrometers, like those available in the PSInet database to further improve  
the potential to link microwave signals and plant behaviour (Pierrat et al., 2025; Restrepo-Acevedo et al., 2024). We encourage  
extending the analysis to comparing GNSS NMRI to higher spatial resolution synthetic aperture radar measurements like with  
715 C-band Sentinel-1 and L-band NISAR. Finally, such cross scale studies with microwave measurements of vegetation are  
critical for understanding plant water stress and short-term drought adaptation and tolerance in dryland ecosystems. This study  
namely serves as a first step for scaling and validation activities for the NASA ARID campaign, which is focused on the  
domain of this study in the western U.S. (Feldman et al., 2024).

### Code and data availability

720 The python code is available for peer review and will be posted on a Zenodo DOI. The data are available for review and will  
be posted to a Zenodo DOI upon acceptance of this manuscript. The authors used publicly available PBO H<sub>2</sub>O site NMRI data  
available from Larson et al. (2014) and at [https://www.unavco.org/data/gps-gnss/derived-products/pbo-  
h2o/documentation/documentation.html](https://www.unavco.org/data/gps-gnss/derived-products/pbo-h2o/documentation/documentation.html). Land cover retrievals are available at Potapov et al. (2022) at  
<https://storage.googleapis.com/earthenginepartners-hansen/GLCLU2000-2020/v2/download.html>. SMAP MT-DCA L-band  
725 soil moisture and VOD were obtained from Feldman et al. (2021) at <https://zenodo.org/records/5619583>. AMSR-2 C-band  
and X-band VOD were obtained from the authors of Baur et al. 2019 upon a request. AMSR-2 LPRM is available from de Jeu  
(2013) and at <https://www.earthdata.nasa.gov/data/catalog/ges-disc-lprm-amr2-ds-d-soilm3-001#toc-citation>. The MODIS  
NDVI dataset is available at <https://modis.gsfc.nasa.gov/data/dataproduct/mod13.php>.

### Author contributions

730 A.F.F. conceived the study, led the analysis, and wrote the initial draft. W.K.S. and A.G.K. provided input on the initial study  
design and analysis. M.J.B. provided several critical datasets used in the analysis. All other authors provided comments on the  
study design which was revised in subsequent iterations. All authors performed substantial edits to the manuscript.



### Competing interests

Andrew F. Feldman is currently an associate editor of Biogeosciences. The other authors declare that they have no conflict of  
735 interest.

### Disclaimer

Copernicus Publications remains neutral with regard to jurisdictional claims made in the text, published maps, institutional  
affiliations, or any other geographical representation in this paper. While Copernicus Publications makes every effort to include  
appropriate place names, the final responsibility lies with the authors. Views expressed in the text are those of the authors and  
740 do not necessarily reflect the views of the publisher.

### Acknowledgements

Components of this manuscript were developed and discussed at a breakout session at the PSInet Water Potential Network  
Workshop in 2025 at Indiana University Bloomington involving several authors. The authors thank the NSF EarthScope PBO  
H<sub>2</sub>O network for GNSS NMRI measurements.

### 745 Financial support

A.F.F., W.K.S., and S.P.S. were supported by a grant from the NASA Ecohydrology Program (Grant Number  
80NSSC25K0156) and by funding from the NASA Terrestrial Ecology program for the ARID dryland field campaign. AGK  
was supported by the Alfred P. Sloan Foundation and by the NASA SMAP Science Team (NSSC 80NSSC25K7055).

### 750 References

- Akbar, R., Short Gianotti, D. J., McColl, K. A., Haghighi, E., Salvucci, G. D., and Entekhabi, D.: Estimation of Landscape  
Soil Water Losses from Satellite Observations of Soil Moisture, *J. Hydrometeorol.*, 19, 871–889, <https://doi.org/10.1175/JHM-D-17-0200.1>, 2018.
- Allred, B. W., Creutzburg, M. K., Carlson, J. C., Cole, C. J., Dovichin, C. M., Duniway, M. C., Jones, M. O., Maestas, J. D.,  
755 Naugle, D. E., Nauman, T. W., Okin, G. S., Reeves, M. C., Rigge, M., Savage, S. L., Twidwell, D., Uden, D. R., and Zhou,  
B.: Guiding principles for using satellite-derived maps in rangeland management, *Rangelands*, 44, 78–86,  
<https://doi.org/10.1016/j.rala.2021.09.004>, 2022.
- Anderegg, W. R. L., Trugman, A. T., Badgley, G., Konings, A. G., and Shaw, J.: Divergent forest sensitivity to repeated



- extreme droughts, *Nat. Clim. Chang.*, 10, 1091–1095, <https://doi.org/10.1038/s41558-020-00919-1>, 2020.
- 760 Anoop, S., Venkata Ramana, M., Karmakar, S., and Ghosh, S.: Evaluating pulse-reserve characteristics of Soil-Plant continuum in India using remote sensing, *J. Hydrol.*, 632, 130913, <https://doi.org/10.1016/j.jhydrol.2024.130913>, 2024.
- Asgarimehr, M., Entekhabi, D., and Camps, A.: Diurnal Vegetation Moisture Cycle in the Amazon and Response to Water Stress, *Geophys. Res. Lett.*, 51, <https://doi.org/10.1029/2024GL111462>, 2024.
- Baur, M. J., Jagdhuber, T., Feldman, A. F., Akbar, R., and Entekhabi, D.: Estimation of relative canopy absorption and scattering at L-, C- and X-bands, *Remote Sens. Environ.*, 233, <https://doi.org/10.1016/j.rse.2019.111384>, 2019.
- 765 Baur, M. J., Jagdhuber, T., Feldman, A. F., Chaparro, D., Piles, M., Entekhabi, D., and Val, U. De: Time-variations of zeroth-order vegetation absorption and scattering at L-band, *Remote Sens. Environ.*, 267, 112726, 2021.
- Brandt, M., Wigneron, J. P., Chave, J., Tagesson, T., Penuelas, J., Ciais, P., Rasmussen, K., Tian, F., Mbow, C., Al-Yaari, A., Rodriguez-Fernandez, N., Schurgers, G., Zhang, W., Chang, J., Kerr, Y., Verger, A., Tucker, C., Mialon, A., Rasmussen, L.
- 770 V., Fan, L., and Fensholt, R.: Satellite passive microwaves reveal recent climate-induced carbon losses in African drylands, *Nat. Ecol. Evol.*, 2, 827–835, <https://doi.org/10.1038/s41559-018-0530-6>, 2018.
- Briske, D. D., Archer, S. R., Burchfield, E., Burnidge, W., Derner, J. D., Gosnell, H., Hatfield, J., Kazanski, C. E., Khalil, M., Lark, T. J., Nagler, P., Sala, O., Sayre, N. F., and Stackhouse-Lawson, K. R.: Supplying ecosystem services on US rangelands, *Nat. Sustain.*, 6, 1524–1532, <https://doi.org/10.1038/s41893-023-01194-6>, 2023.
- 775 Burns, S. P., Humphrey, V., Gutmann, E. D., Raleigh, M. S., Bowling, D. R., and Blanken, P. D.: Using GNSS-based vegetation optical depth, tree sway motion, and eddy covariance to examine evaporation of canopy-intercepted rainfall in a subalpine forest, *Biogeosciences*, 22, 5741–5769, <https://doi.org/10.5194/bg-22-5741-2025>, 2025.
- Chan, S. K., Bindlish, R., O'Neill, P. E., Njoku, E., Jackson, T., Colliander, A., Chen, F., Burgin, M., Dunbar, S., Piepmeier, J., Yueh, S., Entekhabi, D., Cosh, M. H., Caldwell, T., Walker, J., Wu, X., Berg, A., Rowlandson, T., Pacheco, A., McNairn,
- 780 H., Thibeault, M., Martinez-Fernandez, J., Gonzalez-Zamora, A., Seyfried, M., Bosch, D., Starks, P., Goodrich, D., Prueger, J., Palecki, M., Small, E. E., Zreda, M., Calvet, J. C., Crow, W. T., and Kerr, Y.: Assessment of the SMAP Passive Soil Moisture Product, *IEEE Trans. Geosci. Remote Sens.*, 54, 4994–5007, <https://doi.org/10.1109/TGRS.2016.2561938>, 2016.
- Chaparro, D., Piles, M., Vall-Ilossera, M., Camps, A., Konings, A. G., and Entekhabi, D.: L-band vegetation optical depth seasonal metrics for crop yield assessment, *Remote Sens. Environ.*, 212, 249–259, <https://doi.org/10.1016/j.rse.2018.04.049>,
- 785 2018.
- Chaparro, D., Feldman, A. F., Chaubell, M. J., Yueh, S. H., and Entekhabi, D.: Robustness of Vegetation Optical Depth Retrievals Based on L-Band Global Radiometry, *IEEE Trans. Geosci. Remote Sens.*, 60, 1–1, <https://doi.org/10.1109/tgrs.2022.3201581>, 2022.
- Chaubell, J., Yueh, S., Entekhabi, D., and Peng, J.: Resolution enhancement of SMAP radiometer data using the Backus Gilbert optimum interpolation technique, *Int. Geosci. Remote Sens. Symp.*, 2016-Novem, 284–287, <https://doi.org/10.1109/IGARSS.2016.7729065>, 2016.
- 790 Chen, Q., Won, D., Akos, D. M., and Small, E. E.: Vegetation Sensing Using GPS Interferometric Reflectometry: Experimental



- Results with a Horizontally Polarized Antenna, *IEEE J. Sel. Top. Appl. Earth Obs. Remote Sens.*, 9, 4771–4780, <https://doi.org/10.1109/JSTARS.2016.2565687>, 2016.
- 795 Colliander, A., Jackson, T. J., Bindlish, R., Chan, S., Das, N., Kim, S. B., Cosh, M. H., Dunbar, R. S., Dang, L., Pashaian, L., Asanuma, J., Aida, K., Berg, A., Rowlandson, T., Bosch, D., Caldwell, T., Caylor, K., Goodrich, D., al Jassar, H., Lopez-Baeza, E., Martínez-Fernández, J., González-Zamora, A., Livingston, S., McNairn, H., Pacheco, A., Moghaddam, M., Montzka, C., Notarnicola, C., Niedrist, G., Pellarin, T., Prueger, J., Pulliainen, J., Rautiainen, K., Ramos, J., Seyfried, M., Starks, P., Su, Z., Zeng, Y., van der Velde, R., Thibeault, M., Dorigo, W., Vreugdenhil, M., Walker, J. P., Wu, X., Monerris, A., O'Neill, P. E., Entekhabi, D., Njoku, E. G., and Yueh, S.: Validation of SMAP surface soil moisture products with core validation sites, *Remote Sens. Environ.*, 191, 215–231, <https://doi.org/10.1016/j.rse.2017.01.021>, 2017.
- 800 Colliander, A., Cosh, M. H., Misra, S., Jackson, T. J., Crow, W. T., Powers, J., McNairn, H., Bullock, P., Berg, A., Magagi, R., Gao, Y., Bindlish, R., Williamson, R., Ramos, I., Latham, B., O'Neill, P., and Yueh, S.: Comparison of high-resolution airborne soil moisture retrievals to SMAP soil moisture during the SMAP validation experiment 2016 (SMAPVEX16), *Remote Sens. Environ.*, 227, 137–150, <https://doi.org/10.1016/j.rse.2019.04.004>, 2019.
- 805 Collins, S. L., Belnap, J., Grimm, N. B., Rudgers, J. A., Dahm, C. N., D'Odorico, P., Litvak, M., Natvig, D. O., Peters, D. C., Pockman, W. T., Sinsabaugh, R. L., and Wolf, B. O.: A Multiscale, Hierarchical Model of Pulse Dynamics in Arid-Land Ecosystems, *Annu. Rev. Ecol. Evol. Syst.*, 45, 397–419, <https://doi.org/10.1146/annurev-ecolsys-120213-091650>, 2014.
- Crow, W. T. and Feldman, A. F.: Vegetation signal crosstalk present in official SMAP surface soil moisture retrievals, *Remote Sens. Environ.*, 316, 114466, <https://doi.org/10.1016/j.rse.2024.114466>, 2025.
- 810 Dong, J., Crow, W. T., and Bindlish, R.: The Error Structure of the SMAP Single and Dual Channel Soil Moisture Retrievals, *Geophys. Res. Lett.*, 45, 758–765, <https://doi.org/10.1002/2017GL075656>, 2018.
- Ebtehaj, A. and Bras, R. L.: A physically constrained inversion for super-resolved passive microwave retrieval of soil moisture and vegetation water content in L-band, *Remote Sens. Environ.*, 233, 111346, 2019.
- 815 Evans, S. G., Small, E. E., and Larson, K. M.: Comparison of vegetation phenology in the western USA determined from reflected GPS microwave signals and NDVI, *Int. J. Remote Sens.*, 35, 2996–3017, <https://doi.org/10.1080/01431161.2014.894660>, 2014.
- Feldman, A. F.: Emerging Methods to Validate Remotely Sensed Vegetation Water Content, *Geophys. Res. Lett.*, 51, e2024GL110505, <https://doi.org/10.1029/2024GL110505>, 2024.
- 820 Feldman, A. F., Akbar, R., and Entekhabi, D.: Characterization of higher-order scattering from vegetation with SMAP measurements, *Remote Sens. Environ.*, 219, 324–338, <https://doi.org/10.1016/j.rse.2018.10.022>, 2018.
- Feldman, A. F., Chaparro, D., and Entekhabi, D.: Error Propagation in Microwave Soil Moisture and Vegetation Optical Depth Retrievals, *IEEE J. Sel. Top. Appl. Earth Obs. Remote Sens.*, 14, 11311–11323, 2021a.
- Feldman, A. F., Chulakadabba, A., Short Gianotti, D. J., and Entekhabi, D.: Landscape-Scale Plant Water Content and Carbon Flux Behavior Following Moisture Pulses: From Dryland to Mesic Environments, *Water Resour. Res.*, 57, e2020WR027592, <https://doi.org/10.1029/2020WR027592>, 2021b.
- 825



- Feldman, A. F., Short Gianotti, D. J., Konings, A. G., Gentine, P., and Entekhabi, D.: Patterns of plant rehydration and growth following pulses of soil moisture availability, *Biogeosciences*, 18, 831–847, <https://doi.org/10.5194/bg-2020-380>, 2021c.
- Feldman, A. F., Konings, A., Piles, M., and Entekhabi, D.: The Multi-Temporal Dual Channel Algorithm (MT-DCA) (Version 5) [Data set], Zenodo, <https://doi.org/https://doi.org/10.5281/zenodo.5619583>, 2021d.
- Feldman, A. F., Reed, S., Amaral, C., Babst-kostecka, A., Babst, F., Biederman, J. A., Devine, C. J., Fu, Z., Green, J. K., Jessica, S., Hanan, N. P., Kokaly, R. F., Litvak, M., Macbean, N., Ojima, D., Poulter, B., Scott, R. L., Smith, W. K., Robert, J., Tucker, C. J., Wang, L., Watts, J., Wessels, K., Zhang, F., and Zhang, W.: Adaptation and Response in Drylands (ARID): Community Insights for Scoping a NASA Terrestrial Ecology Field Campaign in Drylands, *Earth's Futur.*, 12, e2024EF004811, <https://doi.org/10.1029/2024EF004811>, 2024.
- Felton, A. J., Fisher, J. B., Hufkens, K., Purdy, A. J., Spawn-lee, S. A., Duloisy, L. F., and Goldsmith, G. R.: Global estimates of the storage and transit time of water through vegetation, *Nat. Water*, <https://doi.org/10.1038/s44221-024-00365-9>, 2024.
- Gao, L., Sadeghi, M., Feldman, A. F., and Ebtehaj, A.: A Spatially Constrained Multichannel Algorithm for Inversion of a First-Order Microwave Emission Model at L-Band, *IEEE Trans. Geosci. Remote Sens.*, 1–13, <https://doi.org/10.1109/tgrs.2020.2987490>, 2020.
- Gentine, P., Green, J. K., Guérin, M., Humphrey, V., Seneviratne, S. I., Zhang, Y., and Zhou, S.: Coupling between the terrestrial carbon and water cycles—a review, *Environ. Res. Lett.*, 14, 083003, <https://doi.org/10.1088/1748-9326/ab22d6>, 2019.
- Ghosh, A., Farhad, M. M., Boyd, D., and Kurum, M.: A UGV-Based Forest Vegetation Optical Depth Mapping Using GNSS Signals, *IEEE J. Sel. Top. Appl. Earth Obs. Remote Sens.*, PP, 1–14, <https://doi.org/10.1109/jstars.2024.3365798>, 2024.
- Ghosh, A., Farhad, M. M., Hoque, M. E., Boyd, D. R., Bourgeau-Chavez, L., Cosh, M. H., Colliander, A., and Kurum, M.: Estimating Vegetation Optical Depth with Mobile GNSS Transmissiometry in Temperate Forests During SMAPVEX22, *IEEE J. Sel. Top. Appl. Earth Obs. Remote Sens.*, 18, 6451–6463, <https://doi.org/10.1109/JSTARS.2025.3541182>, 2025.
- Good, S. P., Noone, D., and Bowen, G.: Hydrologic connectivity constrains partitioning of global terrestrial water fluxes, *Science (80-. )*, 349, 175–177, <https://doi.org/10.1126/science.aaa5931>, 2015.
- Green, J. K., Konings, A. G., Alemohammad, S. H., Berry, J., Entekhabi, D., Kolassa, J., Lee, J. E., and Gentine, P.: Regionally strong feedbacks between the atmosphere and terrestrial biosphere, *Nat. Geosci.*, 10, 410–414, <https://doi.org/10.1038/ngeo2957>, 2017.
- Hajj, M. El, Baghdadi, N., Wigneron, J. P., Zribi, M., Albergel, C., Calvet, J. C., and Fayad, I.: First vegetation optical depth mapping from Sentinel-1 C-band SAR data over crop fields, *Remote Sens.*, 11, <https://doi.org/10.3390/rs11232769>, 2019.
- Holtzman, N., Anderegg, L., Kraatz, S., Mavrovic, A., Sonnentag, O., Pappas, C., Cosh, M., Langlois, A., Lakhankar, T., Tesser, D., Steiner, N., Colliander, A., Roy, A., and Konings, A.: L-band vegetation optical depth as an indicator of plant water potential in a temperate deciduous forest stand, *Biogeosciences*, 18, 739–753, <https://doi.org/10.5194/bg-2020-373>, 2021.
- Humphrey, V. and Frankenberg, C.: Continuous ground monitoring of vegetation optical depth and water content with GPS signals, *Biogeosciences*, 20, 1789–1811, <https://doi.org/10.5194/bg-20-1789-2023>, 2023.



- Jackson, T. J. and Schmugge, T. J.: Vegetation effects on the microwave emission of soils, *Remote Sens. Environ.*, 36, 203–212, [https://doi.org/10.1016/0034-4257\(91\)90057-D](https://doi.org/10.1016/0034-4257(91)90057-D), 1991.
- de Jeu, R.: AMSR2/GCOM-W1 surface soil moisture (LPRM) L3 1 day 10 km x 10 km descending V001 [Data set]. NASA Goddard Earth Sciences Data and Information Services Center. <https://doi.org/10.5067/SITUTTDUKYZE> Date Accessed: 2025-04-15, 2013.
- 865 Jones, M. O., Kimball, J. S., Small, E. E., and Larson, K. M.: Comparing land surface phenology derived from satellite and GPS network microwave remote sensing, *Int. J. Biometeorol.*, 58, 1305–1315, <https://doi.org/10.1007/s00484-013-0726-z>, 2014.
- Kesselring, J., Humphrey, V., Niederberger, M., and Feigenwinter, I.: Divergence between in situ and satellite-based estimates of forest canopy water content, *Remote Sens. Environ.*, 332, 115097, <https://doi.org/10.1016/j.rse.2025.115097>, 2025.
- 870 Kilic, L., Prigent, C., Aires, F., Boutin, J., Heygster, G., Tonboe, R. T., Roquet, H., Jimenez, C., and Donlon, C.: Expected Performances of the Copernicus Imaging Microwave Radiometer (CIMR) for an All-Weather and High Spatial Resolution Estimation of Ocean and Sea Ice Parameters, *J. Geophys. Res. Ocean.*, 123, 7564–7580, <https://doi.org/10.1029/2018JC014408>, 2018.
- 875 Konings, A. G. and Gentine, P.: Global variations in ecosystem-scale isohydricity, *Glob. Chang. Biol.*, 23, 891–905, <https://doi.org/10.1111/gcb.13389>, 2017.
- Konings, A. G., McColl, K. A., Piles, M., and Entekhabi, D.: How many parameters can be maximally estimated from a set of measurements?, *IEEE Geosci. Remote Sens. Lett.*, 12, 1081–1085, <https://doi.org/10.1109/LGRS.2014.2381641>, 2015.
- Konings, A. G., Piles, M., Rotzer, K., McColl, K. A., Chan, S. K., and Entekhabi, D.: Vegetation optical depth and scattering albedo retrieval using time series of dual-polarized L-band radiometer observations, *Remote Sens. Environ.*, 172, 178–189, <https://doi.org/10.1016/j.rse.2015.11.009>, 2016.
- 880 Konings, A. G., Piles, M., Das, N., and Entekhabi, D.: L-band vegetation optical depth and effective scattering albedo estimation from SMAP, *Remote Sens. Environ.*, 198, 460–470, <https://doi.org/10.1016/j.rse.2017.06.037>, 2017.
- Konings, A. G., Rao, K., and Steele-Dunne, S. C.: Macro to micro: microwave remote sensing of plant water content for physiology and ecology, *New Phytol.*, 223, 1166–1172, <https://doi.org/10.1111/nph.15808>, 2019.
- 885 Kurum, M., Lang, R. H., O’Neill, P. E., Joseph, A. T., Jackson, T. J., and Cosh, M. H.: A first-order radiative transfer model for microwave radiometry of forest canopies at L-band, *IEEE Trans. Geosci. Remote Sens.*, 49, 3167–3179, <https://doi.org/10.1109/TGRS.2010.2091139>, 2011.
- Kurum, M., Farhad, M. M., and Boyd, D.: GNSS TRANSMISSOMETRY (GNSS-T): MODELING PROPAGATION OF GNSS SIGNALS THROUGH FOREST CANOPY, *IEEE Int. Geosci. Remote Sens. Symp.*, 4695–4698, 2022.
- 890 Larson, K. M.: GPS interferometric reflectometry: applications to surface soil moisture, snow depth, and vegetation water content in the western United States, *Wiley Interdiscip. Rev. Water*, 3, 775–787, <https://doi.org/10.1002/wat2.1167>, 2016.
- Larson, K. M. and Small, E. E.: Normalized microwave reflection index: A vegetation measurement derived from GPS networks, *IEEE J. Sel. Top. Appl. Earth Obs. Remote Sens.*, 7, 1501–1511, <https://doi.org/10.1109/JSTARS.2014.2300116>,



- 895 2014.  
Li, S. and Sawada, Y.: Soil moisture-vegetation interaction from near-global in-situ soil moisture measurements, *Environ. Res. Lett.*, 17, 114028, <https://doi.org/10.1088/1748-9326/ac9c1f>, 2022.
- Liu, Y., Holtzman, N., and Konings, A.: Global ecosystem-scale plant hydraulic traits retrieved using model-data fusion, *Hydrol. Earth Syst. Sci.*, 25, 2399–2417, <https://doi.org/10.5194/hess-2020-649>, 2021.
- 900 McColl, K. A., Wang, W., Peng, B., Akbar, R., Short Gianotti, D. J., Lu, H., Pan, M., and Entekhabi, D.: Global characterization of surface soil moisture drydowns, *Geophys. Res. Lett.*, 44, 3682–3690, <https://doi.org/10.1002/2017GL072819>, 2017.
- Meyer, T., Weihermüller, L., Vereecken, H., and Jonard, F.: Vegetation optical depth and soil moisture retrieved from L-band radiometry over the growth cycle of a winter wheat, *Remote Sens.*, 10, <https://doi.org/10.3390/rs10101637>, 2018.
- 905 Moghaddam, M., Saatchi, S., and Cuenca, R. H.: Estimating subcanopy soil moisture with radar, *J. Geophys. Res. Atmos.*, 105, 14899–14911, <https://doi.org/10.1029/2000JD900058>, 2000.
- Momen, M., Wood, J. D., Novick, K. A., Pangle, R., Pockman, W. T., McDowell, N. G., and Konings, A. G.: Interacting Effects of Leaf Water Potential and Biomass on Vegetation Optical Depth, *J. Geophys. Res. Biogeosciences*, 122, 3031–3046, <https://doi.org/10.1002/2017JG004145>, 2017.
- 910 Olivares-cabello, C., Chaparro, D., Vall-llossera, M., Member, S., Camps, A., López-martínez, C., and Member, S.: Global Unsupervised Assessment of Multifrequency Vegetation Optical Depth Sensitivity to Vegetation Cover, *IEEE J. Sel. Top. Appl. Earth Obs. Remote Sens.*, 16, 538–552, <https://doi.org/10.1109/JSTARS.2022.3226001>, 2023.
- Orland, E., McCabe, T. D., Chen, Y., Scholten, R. C., Becker, Z., Loehman, R. A., Randerson, J. T., Coffield, S. R., Liu, T., and Shiklomanov, A. N.: Near real-time indicators of burn severity in the western U.S. from active fire tracking, *Fire Ecol.*, 915 21, 2025.
- Owe, M., de Jeu, R., and Holmes, T.: Multisensor historical climatology of satellite-derived global land surface moisture, *J. Geophys. Res. Earth Surf.*, 113, 1–17, <https://doi.org/10.1029/2007JF000769>, 2008.
- Pan, Y., Ren, C., Liang, Y., Zhang, Z., and Shi, Y.: Inversion of surface vegetation water content based on GNSS-IR and MODIS data fusion, *Satell. Navig.*, 1, 1–15, <https://doi.org/10.1186/s43020-020-00021-z>, 2020.
- 920 Pierrat, Z. A., Magney, T. S., Richardson, W. P., Runkle, B. R. K., Diehl, J. L., Yang, X., Woodgate, W., Smith, W. K., Johnston, M. R., Ginting, Y. R. S., Koren, G., Albert, L. P., Kibler, C. L., Morgan, B. E., Barnes, M., Uscanga, A., Devine, C., Javadian, M., Meza, K., Julitta, T., Tagliabue, G., Dannenberg, M. P., Antala, M., Wong, C. Y. S., Santos, A. L. D., Hufkens, K., Marrs, J. K., Stovall, A. E. L., Liu, Y., Fisher, J. B., Gamon, J. A., and Cawse-Nicholson, K.: Proximal remote sensing: an essential tool for bridging the gap between high-resolution ecosystem monitoring and global ecology, *New Phytol.*, 925 419–436, <https://doi.org/10.1111/nph.20405>, 2025.
- Potapov, P., Hansen, M. C., Pickens, A., Hernandez-serna, A., Tyukavina, A., Turubanova, S., Zalles, V., Li, X., and Khan, A.: The Global 2000-2020 Land Cover and Land Use Change Dataset Derived From the Landsat Archive : First Results, *Front. Remote Sens.*, 3, 1–22, <https://doi.org/10.3389/frsen.2022.856903>, 2022.



- Restrepo-Acevedo, A. M., Guo, J. S., Kannenberg, S. A., Benson, M. C., Beverly, D., Diaz, R., Anderegg, W. R. L., Johnson,  
930 D. M., Koch, G., Konings, A. G., Lowman, L. E. L., Martínez-Vilalta, J., Poyatos, R., Schenk, H. J., Matheny, A. M.,  
McCulloh, K. A., Nippert, J. B., Oliveira, R. S., and Novick, K.: PSInet: A new global water potential network, *Tree Physiol.*,  
44, <https://doi.org/10.1093/treephys/tpae110>, 2024.
- Sala, O. E. and Lauenroth, W. K.: Small Rainfall Events: An Ecological Role in Semiarid Regions, *Oecologia*, 53, 301–304,  
1982.
- 935 Schellenberg, K., Jagdhuber, T., Chaparro, D., Binks, O., Hellwig, F., Dubois, C., Kurum, M., Camps, A., Hartmann, H., and  
Schmullius, C.: Estimating Canopy Interception Water Storage with GNSS-Transmissometry, *Int. Geosci. Remote Sens.*  
*Symp.*, 4507–4510, <https://doi.org/10.1109/IGARSS53475.2024.10641964>, 2024.
- Shen, X., Fan, L., Zuo, T., Cui, T., Wu, J., Ye, N., Brakhasi, F., Wu, X., Zhu, L., Wigneron, J., Walker, J. P., and Zhang, K.:  
Remote Sensing of Environment P-band radiometry for enhanced vegetation optical depth ( VOD ) and soil moisture retrieval  
940 in dense crop canopies, *Remote Sens. Environ.*, 313, 114353, <https://doi.org/10.1016/j.rse.2024.114353>, 2024.
- Small, E. E., Larson, K. M., and Smith, W. K.: Normalized microwave reflection index: Validation of vegetation water content  
estimates from montana grasslands, *IEEE J. Sel. Top. Appl. Earth Obs. Remote Sens.*, 7, 1512–1521,  
<https://doi.org/10.1109/JSTARS.2014.2320597>, 2014.
- Small, E. E., Roesler, C. J., and Larson, K. M.: Vegetation response to the 2012-2014 California drought from GPS and optical  
945 measurements, *Remote Sens.*, 10, 1–16, <https://doi.org/10.3390/rs10040630>, 2018.
- Smith, W. K., Dannenberg, M. P., Yan, D., Herrmann, S., Barnes, M. L., Barron-Gafford, G. A., Biederman, J. A., Ferrenberg,  
S., Fox, A. M., Hudson, A., Knowles, J. F., MacBean, N., Moore, D. J. P., Nagler, P. L., Reed, S. C., Rutherford, W. A., Scott,  
R. L., Wang, X., and Yang, J.: Remote sensing of dryland ecosystem structure and function: Progress, challenges, and  
opportunities, *Remote Sens. Environ.*, 233, <https://doi.org/10.1016/j.rse.2019.111401>, 2019.
- 950 Taylor, C. M., De Jeu, R. A. M., Harris, P. P., Dorigo, W. A., and Africa, W.: Afternoon rain more likely over drier soils,  
*Nature*, 489, 423–426, <https://doi.org/10.1038/nature11377>, 2012.
- Tian, F., Wigneron, J.-P., Ciais, P., Chave, J., Ogée, J., Peñuelas, J., Ræbild, A., Domec, J.-C., Tong, X., Brandt, M., Mialon,  
A., Rodriguez-Fernandez, N., Tagesson, T., Al-Yaari, A., Kerr, Y., Chen, C., Myneni, R. B., Zhang, W., Ardö, J., and Fensholt,  
R.: Coupling of ecosystem-scale plant water storage and leaf phenology observed by satellite, *Nat. Ecol. Evol.*, 2, 1428–1435,  
955 <https://doi.org/10.1038/s41559-018-0630-3>, 2018.
- Tucker, C. J.: Red and photographic infrared linear combinations for monitoring vegetation, *Remote Sens. Environ.*, 8, 127–  
150, [https://doi.org/10.1016/0034-4257\(79\)90013-0](https://doi.org/10.1016/0034-4257(79)90013-0), 1979.
- Tuttle, S. E. and Salvucci, G. D.: Confounding factors in determining causal soil moisture-precipitation feedback, *Water  
Resour. Res.*, 5531–5544, <https://doi.org/10.1002/2016WR019869>, 2017.
- 960 Wang, L., Good, S. P., and Caylor, K. K.: Global synthesis of vegetation control on evapotranspiration partitioning, *Geophys.*  
*Res. Lett.*, 41, 6753–6757, <https://doi.org/10.1002/2014GL061439>.Received, 2014.
- Wang, X., Dannenberg, M. P., Yan, D., Jones, M. O., Kimball, J. S., Moore, D. J. P., van Leeuwen, W. J. D., Didan, K., and



- Smith, W. K.: Globally Consistent Patterns of Asynchrony in Vegetation Phenology Derived From Optical, Microwave, and Fluorescence Satellite Data, *J. Geophys. Res. Biogeosciences*, 125, 1–15, <https://doi.org/10.1029/2020JG005732>, 2020.
- 965 Wigneron, J. P., Jackson, T. J., O'Neill, P., De Lannoy, G., de Rosnay, P., Walker, J. P., Ferrazzoli, P., Mironov, V., Bircher, S., Grant, J. P., Kurum, M., Schwank, M., Munoz-Sabater, J., Das, N., Royer, A., Al-Yaari, A., Al Bitar, A., Fernandez-Moran, R., Lawrence, H., Mialon, A., Parrens, M., Richaume, P., Delwart, S., and Kerr, Y.: Modelling the passive microwave signature from land surfaces: A review of recent results and application to the L-band SMOS & SMAP soil moisture retrieval algorithms, *Remote Sens. Environ.*, 192, 238–262, <https://doi.org/10.1016/j.rse.2017.01.024>, 2017.
- 970 Xu, X., Konings, A. G., Longo, M., Feldman, A., Xu, L., Saatchi, S., Wu, D., Wu, J., and Moorcroft, P.: Leaf surface water, not plant water stress, drives diurnal variation in tropical forest canopy water content, *New Phytol.*, <https://doi.org/10.1111/nph.17254>, 2021.
- Yao, Y., Humphrey, V., Konings, A. G., Wang, Y., Yin, Y., Holtzman, N., Wood, J. D., On, Y. B., and Frankenberg, C.: Investigating Diurnal and Seasonal Cycles of Vegetation Optical Depth Retrieved From GNSS Signals in a Broadleaf Forest, *Geophys. Res. Lett.*, <https://doi.org/10.1029/2023GL107121>, 2024.
- 975 Yebra, M., Dennison, P. E., Chuvieco, E., Riaño, D., Zylstra, P., Hunt, E. R., Danson, F. M., Qi, Y., and Jurdao, S.: Remote Sensing of Environment A global review of remote sensing of live fuel moisture content for fire danger assessment : Moving towards operational products, *Remote Sens. Environ.*, 136, 455–468, <https://doi.org/10.1016/j.rse.2013.05.029>, 2013.
- Zeng, Y., Hao, D., Huete, A., Dechant, B., Berry, J., Chen, J. M., Joiner, J., Frankenberg, C., Bond-Lamberty, B., Ryu, Y.,
- 980 Xiao, J., Asrar, G. R., and Chen, M.: Optical vegetation indices for monitoring terrestrial ecosystems globally, *Nat. Rev. Earth Environ.*, 3, 477–493, <https://doi.org/10.1038/s43017-022-00298-5>, 2022.
- Zhang, S., Roussel, N., Boniface, K., Cuong Ha, M., Frappart, F., Darrozes, J., Baup, F., and Calvet, J. C.: Use of reflected GNSS SNR data to retrieve either soil moisture or vegetation height from a wheat crop, *Hydrol. Earth Syst. Sci.*, 21, 4767–4784, <https://doi.org/10.5194/hess-21-4767-2017>, 2017.
- 985 Zhang, Y., Zhou, S., Gentine, P., and Xiao, X.: Can vegetation optical depth reflect changes in leaf water potential during soil moisture dry-down events?, *Remote Sens. Environ.*, 234, 111451, 2019.
- Zhao, M., Humphrey, V., Feldman, A. F., and Konings, A. G.: Temperature Is Likely an Important Omission in Interpreting Vegetation Optical Depth, *Geophys. Res. Lett.*, 51, <https://doi.org/10.1029/2024GL110094>, 2024.
- Zotta, R., Moesinger, L., Schalie, R. Van Der, Vreugdenhil, M., Preimesberger, W., Frederikse, T., de Jeu, R., and Dorigo, W.
- 990 A.: VODCA v2: multi-sensor, multi-frequency vegetation optical depth data for long-term canopy dynamics and biomass monitoring, *Earth Syst. Sci. Data*, 16, 4573–4617, 2024.
- Zotta, R., Jeu, R. De, Francois, N., and Frederikse, T.: Improving AMSR2 vegetation optical depth retrievals via land parameter retrieval model parameter optimisation, *Remote Sens. Environ.*, 335, 2026.